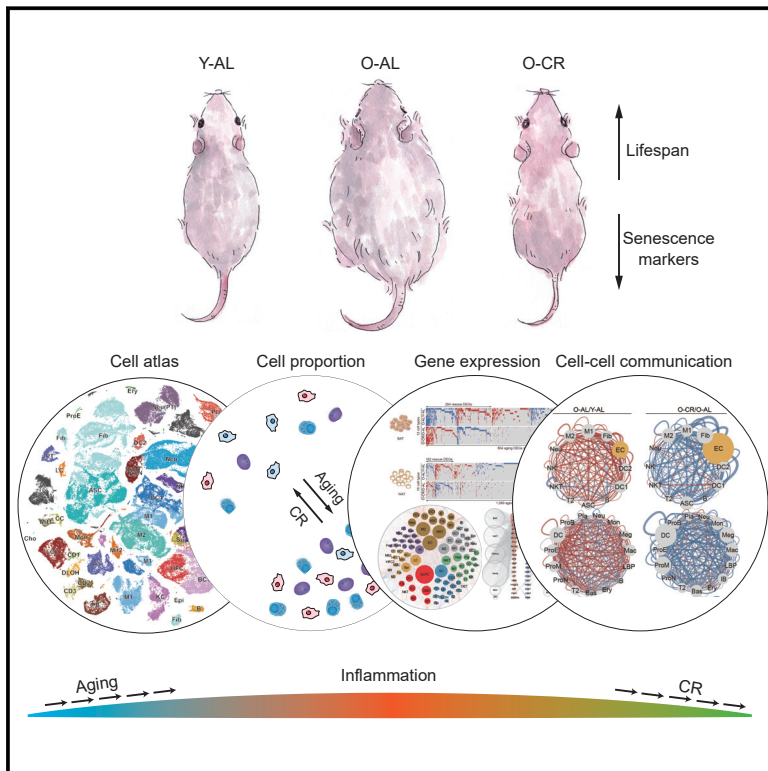


# Caloric Restriction Reprograms the Single-Cell Transcriptional Landscape of *Rattus Norvegicus* Aging

## Graphical Abstract



## Authors

Shuai Ma, Shuhui Sun, Lingling Geng, ..., Weiqi Zhang, Jing Qu, Guang-Hui Liu

## Correspondence

belmonte@salk.edu (J.C.I.B.),  
zhangwq@big.ac.cn (W.Z.),  
qujing@ioz.ac.cn (J.Q.),  
ghliu@ioz.ac.cn (G.-H.L.)

## In Brief

Single-cell transcriptomic analysis in aging rats provides insights into the effects of caloric restriction on different tissue and cell types.

## Highlights

- A multitissue single-cell transcriptomic atlas for aging and CR in a mammal
- CR alleviates aging-related accumulation of pro-inflammatory cells in various tissues
- CR attenuates aging-associated cell-type-specific gene expression changes



# Caloric Restriction Reprograms the Single-Cell Transcriptional Landscape of *Rattus Norvegicus* Aging

Shuai Ma,<sup>1,2,12</sup> Shuhui Sun,<sup>2,12</sup> Lingling Geng,<sup>3,4,12</sup> Moshi Song,<sup>1,5,6,12</sup> Wei Wang,<sup>1,6</sup> Yanxia Ye,<sup>3,5</sup> Qianzhao Ji,<sup>1,6</sup> Zhiran Zou,<sup>1,6</sup> Si Wang,<sup>1,4,5,13</sup> Xiaojuan He,<sup>4</sup> Wei Li,<sup>4</sup> Concepcion Rodriguez Esteban,<sup>7</sup> Xiao Long,<sup>8</sup> Guoji Guo,<sup>9,13</sup> Piu Chan,<sup>4,13</sup> Qi Zhou,<sup>3,5,6,13</sup> Juan Carlos Izpisua Belmonte,<sup>7,\*</sup> Weiqi Zhang,<sup>4,5,6,10,11,\*</sup> Jing Qu,<sup>3,5,6,\*</sup> and Guang-Hui Liu<sup>1,2,4,5,6,14,\*</sup>

<sup>1</sup>State Key Laboratory of Membrane Biology, Institute of Zoology, Chinese Academy of Sciences, Beijing 100101, China

<sup>2</sup>National Laboratory of Biomacromolecules, CAS Center for Excellence in Biomacromolecules, Institute of Biophysics, Chinese Academy of Sciences, Beijing 100101, China

<sup>3</sup>State Key Laboratory of Stem Cell and Reproductive Biology, Institute of Zoology, Chinese Academy of Sciences, Beijing 100101, China

<sup>4</sup>Advanced Innovation Center for Human Brain Protection, and National Clinical Research Center for Geriatric Disorders, Xuanwu Hospital Capital Medical University, Beijing 100053, China

<sup>5</sup>Institute for Stem Cell and Regeneration, Chinese Academy of Sciences, Beijing 100101, China

<sup>6</sup>University of Chinese Academy of Sciences, Beijing 100049, China

<sup>7</sup>Gene Expression Laboratory, Salk Institute for Biological Studies, La Jolla, CA, USA

<sup>8</sup>Division of Plastic Surgery, Peking Union Medical College Hospital, Beijing 100032, China

<sup>9</sup>Center for Stem Cell and Regenerative Medicine, Zhejiang University School of Medicine, Hangzhou 310058, China

<sup>10</sup>Disease Genomics and Individualized Medicine Laboratory, Beijing Institute of Genomics, Chinese Academy of Sciences, Beijing 100101, China

<sup>11</sup>China National Center for Bioinformatics, Beijing 100101, China

<sup>12</sup>These authors contributed equally

<sup>13</sup>Senior author

<sup>14</sup>Lead Contact

\*Correspondence: [belmonte@salk.edu](mailto:belmonte@salk.edu) (J.C.I.B.), [zhangwq@big.ac.cn](mailto:zhangwq@big.ac.cn) (W.Z.), [qujing@ioz.ac.cn](mailto:qujing@ioz.ac.cn) (J.Q.), [gghliu@ioz.ac.cn](mailto:gghliu@ioz.ac.cn) (G.-H.L.)  
<https://doi.org/10.1016/j.cell.2020.02.008>

## SUMMARY

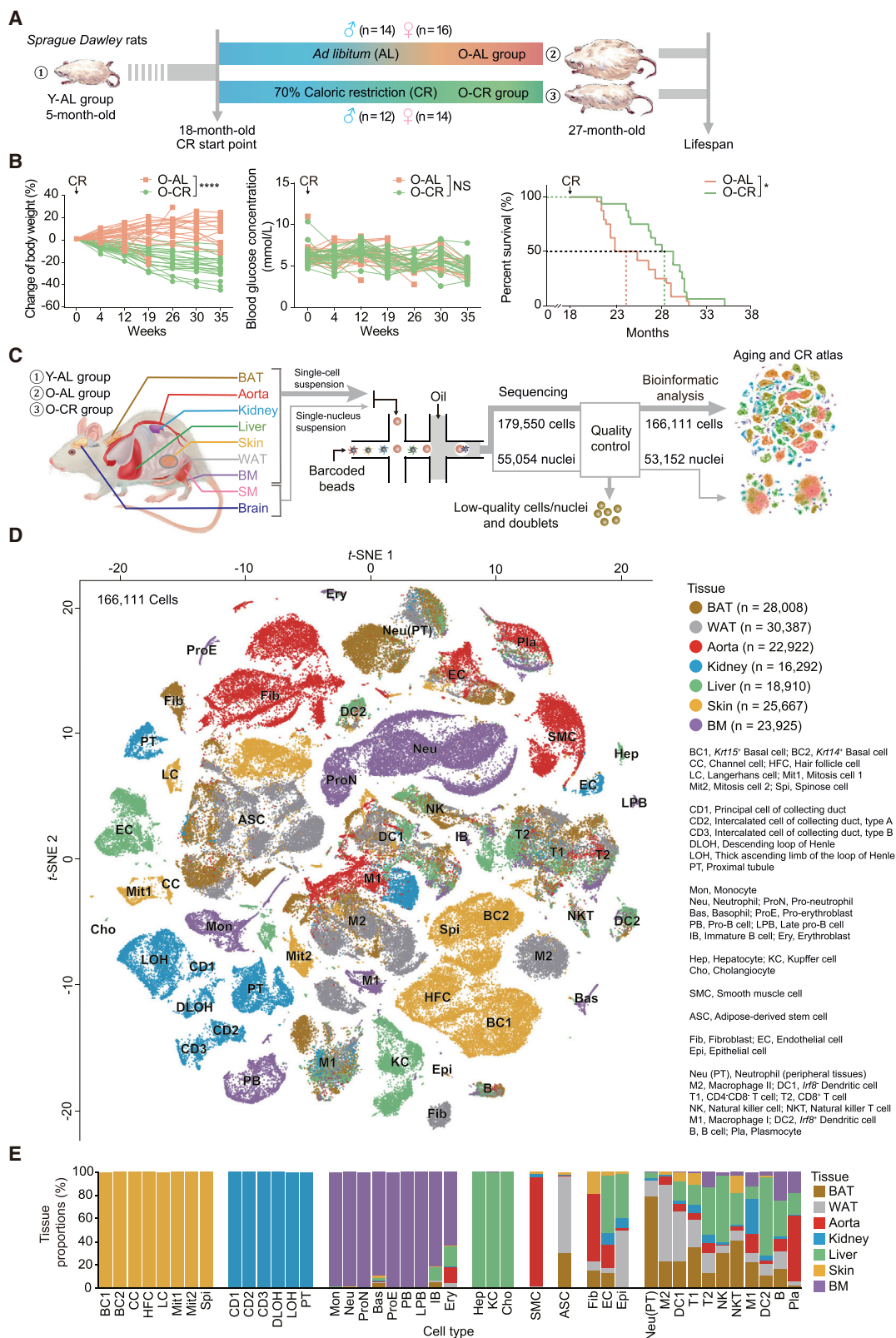
Aging causes a functional decline in tissues throughout the body that may be delayed by caloric restriction (CR). However, the cellular profiles and signatures of aging, as well as those ameliorated by CR, remain unclear. Here, we built comprehensive single-cell and single-nucleus transcriptomic atlases across various rat tissues undergoing aging and CR. CR attenuated aging-related changes in cell type composition, gene expression, and core transcriptional regulatory networks. Immune cells were increased during aging, and CR favorably reversed the aging-disturbed immune ecosystem. Computational prediction revealed that the abnormal cell-cell communication patterns observed during aging, including the excessive proinflammatory ligand-receptor interplay, were reversed by CR. Our work provides multi-tissue single-cell transcriptional landscapes associated with aging and CR in a mammal, enhances our understanding of the robustness of CR as a geroprotective intervention, and uncovers how metabolic intervention can act upon the immune system to modify the process of aging.

## INTRODUCTION

Aging causes a functional decline in multiple tissues of the body and leads to increased susceptibility to various chronic diseases (Campisi et al., 2019; Zhang et al., 2020). Aging-related phenotypes manifest at the organismal, tissue, cellular, and molecular levels (Zhang et al., 2015). Postulated mechanisms of aging include genomic instability, epigenetic alterations, altered intracellular communication, increased chronic inflammation, stem cell exhaustion, and accumulation of senescent cells (López-Otín et al., 2013). Aging elicits distinct responses across different types of cells, tissues, and organs and leads to increased gene expression heterogeneity even within cells of the same type. Due to this complexity, it is necessary to comprehensively compare aging phenotypes and examine regulatory factors across different cell populations in multiple organs.

Several interventions have been proposed to rejuvenate cells and organs, delay the onset of age-associated diseases, and extend healthspan and lifespan, among which caloric restriction (CR) has been recognized as one of the most effective interventions (Fontana and Partridge, 2015). Continued studies on CR, beginning in 1935 with a study in rats by McCay et al. (1935), have consistently shown that CR can facilitate physical fitness, as evidenced by improvements in body mass index, skin condition, liver and kidney function, as well as decreased risk of cardiovascular diseases (Fontana and Partridge, 2015). The inverse





(legend on next page)

relationship observed between caloric intake and lifespan in rodents suggests that CR-induced metabolic reprogramming may be a key event linked to lifespan extension (Pifferi and Aujard, 2019). Studies in yeast, worms, flies, and mice further point to a role for nutrient-responsive signaling molecules, including SIRT1, mTOR, and PGC-1 $\alpha$ , in aging and CR (Fontana and Partridge, 2015; Spindler, 2010). Although previous studies have provided valuable insights into the effects of CR on individual organs (Forni et al., 2017; Fujii et al., 2019), the means by which CR, as a powerful metabolic intervention, rewires aging programs across multiple tissues to extend organismal lifespan is poorly understood.

Despite previous transcriptome studies on aging and CR (Rhoads et al., 2018; Wood et al., 2015; Zou et al., 2017), the construction of high-dimensional molecular profiles across multiple cell populations via traditional molecular biology techniques such as bulk-segregant sequencing (Bulk-seq) remains challenging. The recent development of single-cell RNA sequencing (scRNA-seq) has overcome this limitation, allowing the assessment of transcriptional features across all prevalent cell identities in an organism (Macosko et al., 2015; Tang et al., 2009). With the development of high-throughput single-cell technologies, two atlases of adult mice, covering hundreds of cell types in the whole organism, have recently been reported (Han et al., 2018; Schaum et al., 2018). However, a comprehensive multiorgan aging cell atlas, not to mention a CR cell atlas across body tissues, has not been constructed.

To this end, we performed integrative profiling of multitissue transcriptome to study aging and its modulation by CR at the single-cell level in a mammal, *Rattus norvegicus*. We systematically analyzed more than 210,000 single cells and nuclei across nine types of tissues sampled from young and old rats subjected to *ad libitum* (AL) feeding, and old rats subjected to CR beginning in middle adulthood. The systemic effects of aging and CR on different tissues were evaluated in terms of cell type composition, cell- and tissue-specific molecular programs, regulatory transcription factors (TFs), and cell-cell communication networks. Extensive disturbances in all of these aspects were observed during aging and partially rescued by CR, with the most marked effects observed in adipose and aortic tissues. CR rescued aging-related changes in cell type composition, especially neutrophils, which were increased during aging and reduced by CR in multiple tissues. At the transcriptional level, the changes in more than one-fourth of the differentially expressed genes (DEGs) between young and aged rats, including genes encoding core regulatory transcription factors related to lipid metabolism and immunomodulation, were reversed by

CR. In addition, computational prediction revealed that the aging-related burden in abnormal cell-cell communication may be attenuated by CR. Overall, this work provides a wealth of molecular information about aging and the effect of CR in aging, expands our knowledge of CR as a powerful intervention for aging via multi-tissue single-cell transcriptomic profiling, and highlights key nodes between the immune system and metabolic interventions that may serve to modulate the process of aging.

## RESULTS

### The Effects of CR on Lifespan and Aging Features

Given that “adult-onset CR” (i.e., CR started in middle adulthood) may be more relevant to potential clinical applications than CR started at early ages (Levay et al., 2007), middle-aged rats (18 months old) were evenly matched and randomized to AL or 70% CR diets considering their baseline body weights, food intake, and blood glucose concentrations (Figures 1A and S1A). After 9 months of dietary intervention, the rats in both the AL and CR groups were 27 months of age, analogous to 70 years in humans, and were referred to as the O-AL and O-CR groups, respectively. Rats in both the O-AL and O-CR groups were analyzed in comparison with 5-month-old (young) rats fed AL (referred to as the Y-AL group), approximately analogous to 16-year-old humans.

The body weight of O-CR rats was reduced by an average of one-third ( $32.6\% \pm 3.9\%$ ) of that of O-AL control rats after 9 months of CR, with no effect on serum glucose levels (Figure 1B). CR extended both the median and maximum lifespans of O-CR rats compared with those of O-AL control rats (Figure 1B). In addition, CR exerted profound effects on aging-associated morphological changes in tissues. As visualized by Oil Red O staining, fewer lipid droplets accumulated in the livers of Y-AL and O-CR rats than in those of O-AL control rats (Figure S1B). In addition, fewer small multilocular adipocytes and more large lipid droplets characterized by aged beige adipocytes were found in brown adipose tissue (BAT) of O-AL rats, and these changes were reversed upon CR (Figure S1C). Similarly, the size of adipocytes in white adipose tissue (WAT) was reduced by CR (Figure S1C). Moreover, senescence-associated  $\beta$ -galactosidase (SA- $\beta$ -Gal) staining revealed an accumulation of senescent cells in aged WAT, BAT, liver tissue, and kidney tissue, which was reversed by CR (Figure S1D). Consistent with these results, the level of LINE1-ORF1p, an aging marker associated with genomic instability and senescence-associated secretory phenotypes (SASPs), in WAT and BAT was decreased by CR (Figure S1E) (Childs and van Deursen, 2019). In addition,

### Figure 1. Construction of Rat Cell Atlases by scRNA-Seq

(A) Schematic diagram of rats subjected to a 70% calorie-restricted diet for a 9-month period starting at the age of 18 months. Y-AL, 5-month-old rats fed *ad libitum*; O-AL, 27-month-old rats fed *ad libitum*; O-CR, 27-month-old rats subjected to a 70% calorie-restricted diet beginning at 18 months of age.

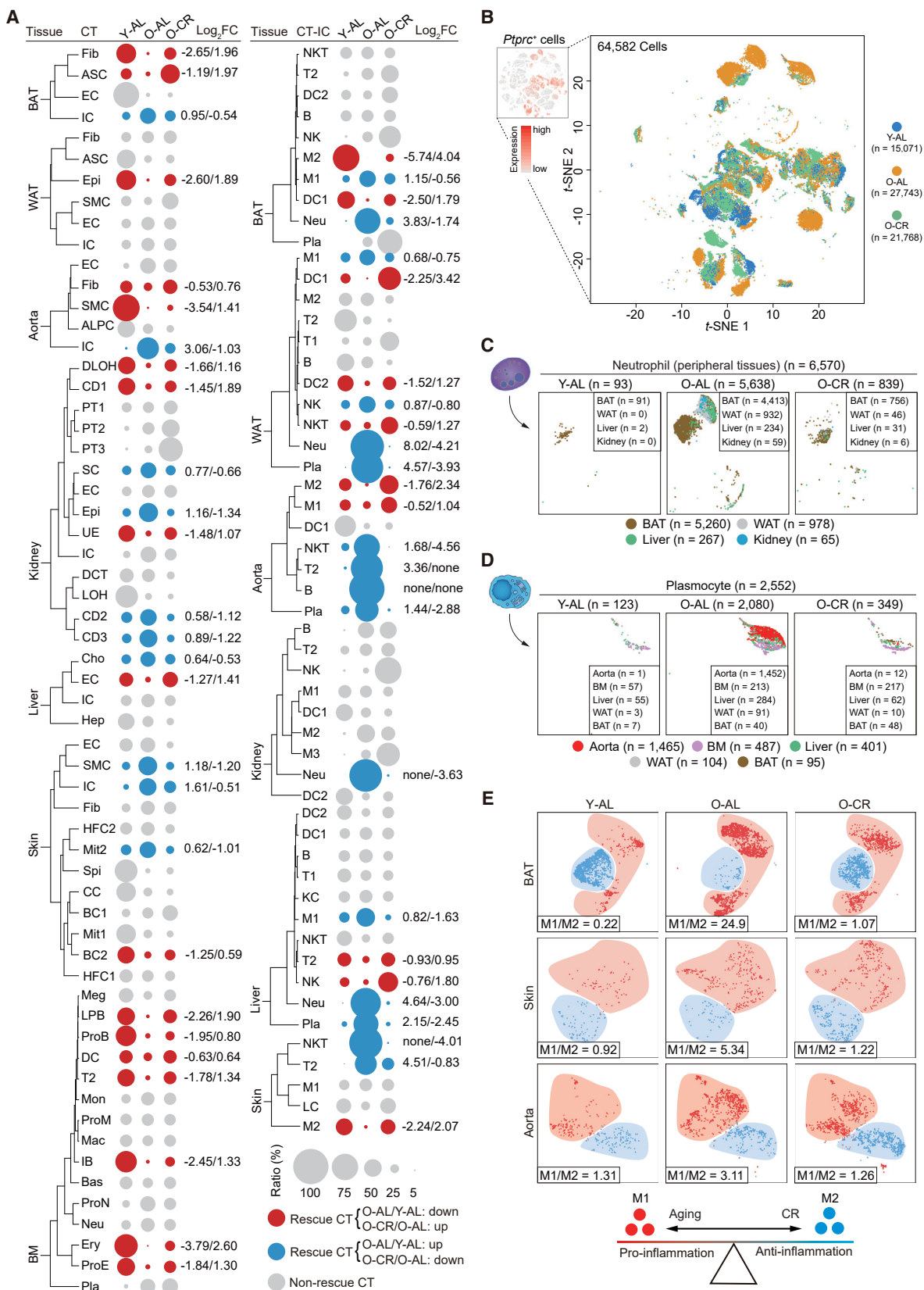
(B) Quantification of the percentage of gained and lost body weight, blood glucose concentration, and survival curves for O-AL (n = 30, 14 male and 16 female rats) and O-CR (n = 26, 12 male and 14 female rats) groups. Two-tailed Student's t tests or log-rank tests were used. The data are shown as means  $\pm$  SEM. \*p < 0.05; \*\*\*\*p < 0.0001; NS, not significant.

(C) Flowchart overview of the scRNA-seq and snRNA-seq methodology.

(D) t-SNE plots showing different cell types across the seven tissues by scRNA-seq.

(E) Proportions of the 42 major cell types in the tissues by scRNA-seq.

See also Figure S1 and Table S1.



(legend on next page)

the accumulation of proinflammatory cytokine tumor necrosis factor- $\alpha$  (TNF $\alpha$ ) in the serum from aged rats was suppressed by CR (Figure S1F). Taken together, our data suggest that moderate CR delays the onset of aging-associated phenotypes and extends the lifespan of rats.

### Construction of Rat Single-Cell Atlases by scRNA-Seq

To understand the effects of aging and CR on the cell type composition and transcriptional profiles of various tissues, we generated single-cell atlases for Y-AL, O-AL, and O-CR rats. BAT, WAT, livers, kidneys, aortas, skin, and bone marrow (BM) were isolated from Y-AL, O-AL, and O-CR rats, processed into single-cell suspensions and loaded into a droplet-forming microfluidic device (see STAR Methods) (Figure 1C). After quality control (see STAR Methods), a total of 166,111 qualified cells were obtained for subsequent analyses (Figures 1C, S1G and Table S1).

To define each cell type, we first processed the sequencing data using the DoubletFinder and Seurat R packages for quality control, normalization, batch effect correction, and clustering (see STAR Methods) and annotated each cell type based on the expression levels of canonical cell-type-specific markers. In total, we identified 109 cell clusters that could be divided into 42 major cell types across the seven tissues (Figures 1D, S1H–S1K, and Table S1). Of these cell types, more than 20 were tissue-specific, such as *Cyp2e1*<sup>+</sup> hepatocytes in the liver and *Pdgfra*<sup>+</sup> adipose-derived stem cells (ASCs) in adipose tissue. In contrast, *Pecam1*<sup>+</sup> endothelial cells (ECs) and *Lum*<sup>+</sup> fibroblasts were present in most tissues, including BAT, WAT, aorta, skin, and liver (Figure 1E). Notably, *Ptprc*<sup>+</sup> cells were found in BM as well as the other six types of tissues we analyzed and were subdivided into 18 immune cell types, including neutrophils, M1 (pro-inflammatory) macrophages (M1), M2 (anti-inflammatory) macrophages (M2), cytotoxic CD8<sup>+</sup> T cells (T2), B cells, and plasmocytes (Figures 1D and 1E) (Papalexi and Satija, 2018). Detailed information on cell type descriptions and marker genes for each type of tissue is available in Table S1. Altogether, we generated a multitissue representation of cellular diversity, constructed a comparative framework and established a cellular roadmap for further studies of aging and CR.

### Reconstitution of the Cellular Ecosystem of Aging by CR

To delineate the cell type composition dynamics during aging and CR, we compared the proportions of each cell type separately across seven tissues between the Y-AL, O-AL, and O-CR groups (Figures 2A and S2). The cell types whose proportions were changed during aging and reversed by CR are shown in Figure 2A (see STAR Methods). Globally, we observed changes in the proportions of various cell types in the O-AL

group compared to the Y-AL group, and many of these changes were rescued by CR (Figures 2A and S3A–3G). For example, the proportions of BC2 (*Krt14*<sup>+</sup> epithelial stem cells) in skin and ASCs in BAT were reduced during aging and increased by CR (Figure 2A), indicating that CR may prevent age-associated stem cell exhaustion, as previously reported (Bi et al., 2018). The decrease in smooth muscle cells (SMCs, *SMA*<sup>+</sup>) in the aged aorta was partially rescued by CR (Figure 2A), consistent with the aging-related increase in apoptotic cells in the middle layer of vascular walls, which was reversed by CR (Figure S3B). These results are in line with those of previous reports indicating that CR reduces the stiffness of aged vessels (Ahmet et al., 2011; Redman et al., 2018). In BM, pro-B (ProB) cells, late pro-B cells (LPB), immature B cells (IB), CD8<sup>+</sup> T cells (T2), dendritic cells (DC, *Irf8*<sup>+</sup>), pro-erythroblasts (ProE), and erythroblasts (Ery) were reduced during aging and effectively replenished by CR (Figure 2A). Combined with the results obtained via fluorescence-activated cell sorting (FACS) (Figure S3D), these data support the idea that CR repopulates lymphocytes and erythroblasts in aged individuals (Contreras et al., 2018; Lomako and Shylo, 2019).

Notably, we observed that the numbers of immune cells (*Ptprc*<sup>+</sup> cells) in multiple tissues except BM were increased during aging and that these increases were prevented by CR (Figures 2B, S3H and S3I). The numbers of neutrophils and plasmocytes were prominently increased during aging and decreased upon CR (Figures 2C and 2D and S3J), and these changes were confirmed by immunostaining of the corresponding tissues (Figures S3E and S3F) (Reckless et al., 2001). Neutrophil accumulation with an inflammatory response has been reported in WAT or liver tissue of both obese and diabetic mice (Talukdar et al., 2012; Trim et al., 2018). Consistent with this observation, we found that the neutrophils residing in peripheral tissues expressed low levels of BM pro-neutrophil markers (*Mki67*<sup>+</sup>/*Lcn2*<sup>+</sup>) and BM neutrophil markers (*Lcn2*<sup>+</sup>) but high levels of the chemotactic factors *Cxcl2*, *Ccl2* (MCP-1), and *Cxcr4* (Figures S3K and S3L). Combined with the pseudotime analysis data, these data suggest that neutrophils might migrate out of the BM and infiltrate into peripheral tissues, including BAT, WAT, liver, and kidney tissues, during aging and that this migration was reversed by CR (Figures S3K and S3L). In addition, increased macrophage infiltration was observed in the liver tissue and WAT of O-AL rats compared to Y-AL rats, and this infiltration was reversed in O-CR rats (Figures 2A and S3G) (Wasinski et al., 2013). More importantly, the ratio of M1 (pro-inflammatory) to M2 (anti-inflammatory) macrophages (an indication of chronic inflammation) was increased in multiple aged tissues and reversed by CR (BAT, skin, and aorta) (Figure 2E), suggesting that CR induces a shift in macrophage polarization from a

### Figure 2. Changes in Cell Proportions during Aging and CR

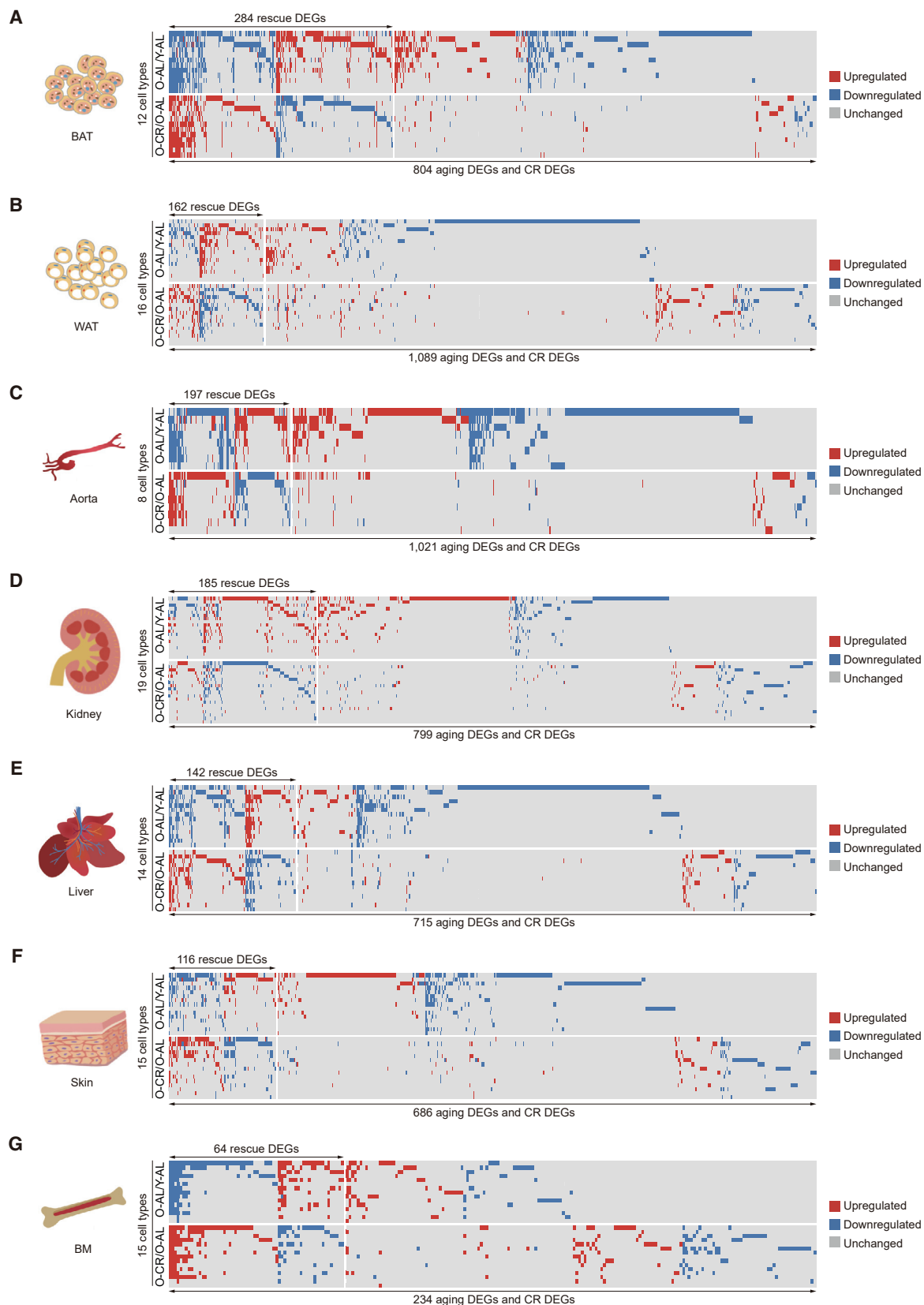
(A) Relative changes in cell ratios in different tissues across the three groups (Y-AL, O-AL, and O-CR). The numbers on the right indicate the Log<sub>2</sub>FC values of the cell ratios (O-AL/Y-AL and O-CR/O-AL). CT, cell type; IC, immune cell.

(B) *t*-SNE plots showing that immune cells accumulated in O-AL tissues. Left, *t*-SNE plot highlighting the *Ptprc*<sup>+</sup> cells, except for the cells from BM, shown in the same layout used in Figure 1D. Right, *t*-SNE plot of immune cells (*Ptprc*<sup>+</sup>) in the Y-AL, O-AL, and O-CR groups.

(C and D) *t*-SNE plots showing the numbers of neutrophils (C) and plasmocytes (D) in the indicated groups (Y-AL, O-AL, and O-CR).

(E) *t*-SNE plots showing changes in the M1/M2 macrophage ratio.

See also Figures S2 and S3.



(legend on next page)

pro-inflammatory to an anti-inflammatory state in various tissues (Liu et al., 2014).

### Reversal of Aging-Related Gene Expression Changes across Tissues by CR

To unveil the molecular events associated with aging and CR, thousands of DEGs between O-AL and Y-AL rats and between O-CR and O-AL rats were identified and referred to as “aging DEGs” and “CR DEGs,” respectively (Figures 3A–3G and 4A and Table S2). Integrative comparative analysis of these DEGs further identified aging DEGs that were partially rescued by CR and thereby referred to as “rescue DEGs” (Figures 3A–3G and 4A; see STAR Methods).

Next, to separate the effects of aging and CR on each tissue, we attributed aging, CR, and rescue DEGs to each tissue type. Strikingly, as shown in the rose diagrams, aorta tissues, BAT, and WAT were among the tissues most strongly affected by both aging and CR based on the number of DEGs (Figure 4B). In contrast, although the cell type composition was changed (Figure 2A), fewer DEGs were detected in BM than in the above-mentioned tissues upon aging and CR (Figures 3A–3G and 4B). These analyses highlight the tissue-specific effects of aging and CR and demonstrate that the multitissue comparison may provide a more comprehensive portrait to better understand the mechanisms of aging and CR. To comprehensively interpret the effects of CR on the global transcriptomic profile, we further analyzed two sets of genes, i.e., upregulated aging DEGs that were further increased by CR and downregulated aging DEGs that were further decreased by CR. These DEGs accounted for only approximately 1.8% of the aging DEGs, suggesting that CR may exert minimal side effects in rats (Figures S4A–S4C).

We next explored the biological implications of aging, CR, and rescue DEGs using Gene Ontology (GO) and pathway analyses (<http://metascape.org>) for each tissue. The commonly downregulated genes across tissues during aging were enriched in vasculature development, cellular response to growth factors, regeneration, and extracellular matrix organization, and their downregulation was antagonized by CR (Figures 4C and S4E–S4G). Aging also led to a synchronous enhancement of multiple pathways involved in the inflammatory response, innate immune response, and positive regulation of cell death, and this enhancement was attenuated by CR (Figures 4C and S4E–S4G). The functional comparative analysis of aging and rescue DEGs among the tissues further supports the role of CR in anti-inflammatory, tissue regeneration, and proangiogenic pathways, all of which are pathways contributing to geroprotection (Fontana and Partridge, 2015).

To determine the common rescue DEGs shared by multiple tissues, we generated Venn diagrams of rescue DEGs in different

tissues and showed that 46 downregulated aging DEGs were reactivated by CR in at least three tissues, while 34 upregulated aging DEGs were suppressed by CR in at least three tissues (frequency,  $\text{freq} \geq 3$ ) (Figure 4D and Table S3). Among these DEGs, *Ybx1* ( $\text{freq} = 5$ ), *Cebpb* ( $\text{freq} = 5$ ), *Klf4* ( $\text{freq} = 3$ ), and *Atf3* ( $\text{freq} = 3$ ) were downregulated during aging and were restored by CR (Figure 4D and Table S3). For example, *Ybx1* was downregulated in six tissues (BAT, WAT, liver, skin, aorta, and BM) during aging and was restored in five tissues (BAT, WAT, liver, aorta, and BM) by CR (Table S3). Notably, *Ybx1*, *Cebpb*, *Klf4*, and *Atf3* have been implicated in diverse cellular processes. *Ybx1* is a DNA/RNA-binding protein that regulates mRNA transcription, packaging, splicing, and translation (Kretov et al., 2019). *Cebpb* is a key transcription factor involved in fat catabolism, tissue regeneration, and life extension in mice (Guo et al., 2015). *Klf4* is an indicator of stem cell capacity and is involved in stem cell maintenance and somatic cell reprogramming (Di Giammartino et al., 2019). *Atf3* is a transcription factor regulating a wide range of host defense-related genes and is important for the maintenance of DNA integrity (Wang et al., 2018). Thus, CR may depend on the restoration of the expression of these factors to reprogram transcriptional signatures across tissues during aging. In contrast, the aging-associated increases in five proinflammatory factors, *S100a9* ( $\text{freq} = 5$ ), *Igkc* ( $\text{freq} = 5$ ), *S100a8* ( $\text{freq} = 4$ ), *Cxcl2* ( $\text{freq} = 3$ ), and *Il1b* ( $\text{freq} = 3$ ), were counteracted by CR (Figure 4D and Table S3). Consistent with these findings, the high level of S100A8 in the serum of aged rats was decreased by CR (Figure S4D). These aging DEGs across tissues that were commonly rescued by CR may represent important biomarkers and targets for intervention by CR.

### Inversion of Aging-Related Cell-Type-Specific Gene Expression Networks by CR

We next sought to define the cell type specificity of these aging, CR, and rescue DEGs across the seven tissues. As indicated by the varied sizes of the circles, the effects of aging and CR were not only tissue-specific but also cell-type-specific (Figure 5A). Globally, aorta-localized proliferative cells (ALPCs), natural killer T cells (NKTs), and neutrophils were the cell types most strongly affected by aging across the seven tissues, while ALPCs, M2, and ECs were the most effectively rescued by CR according to their DEG numbers (Figures 5A and 5B). In terms of tissue specificity, neutrophils, M1, and M2 were the top three cell types most strongly affected by aging in WAT based on the number of aging DEGs; among these cell types, M2 and ECs were more effectively rescued by CR (Figures 5A and 5B). In BAT, NKTs, M2, and ECs were the top three cell types with the most aging DEGs, and interestingly, all were the most effectively rescued by CR (Figures 5A and 5B). In aortic tissue, ALPCs, SMCs, and fibroblasts were the three cell types with the most aging DEGs,

#### Figure 3. Changes in Transcriptional Profiles during Aging and CR

(A–G) Heatmaps showing the distribution of DEGs in each cell type across the seven tissues including BAT (A), WAT (B), aorta (C), kidney (D), liver (E), skin (F), and BM (G). Each row represents one cell type, and each column represents one gene. Red, upregulated ( $\text{LogFC} > 0.5$ , adjusted  $p$  value  $< 0.05$ ); blue, downregulated ( $\text{LogFC} > 0.5$ , adjusted  $p$  value  $< 0.05$ ); gray, unchanged ( $|\text{LogFC}| < 0.5$ ). Aging DEGs are the genes that were changed in the O-AL group compared to the Y-AL group, and CR DEGs are the genes that were changed in the O-CR group compared to the O-AL group. Rescue DEGs are the genes that exhibited the opposite changes in CR DEGs compared to aging DEGs.

See also Table S2.



and ALPCs were the most effectively restored to a younger state by CR (Figures 5A and 5B).

Enrichment analysis further showed that the upregulated rescue DEGs across cell types were enriched in GO terms associated with development, regeneration, the response to growth factors, extracellular matrix organization, and the response to corticosteroids (Figures S4F and S4G). In contrast, the downregulated rescue DEGs across cell types were enriched in GO terms associated with inflammation, the innate immune response, the response to lipopolysaccharide, the response to interleukins, reactive oxygen species (ROS) metabolic processes, and apoptotic signaling pathways (Figures S4F and S4G). These results identified the key cell types affected by aging and CR in various tissues.

Notably, *S100a9*, *S100a8*, and *Igkc* were upregulated in more than 40 cell types during aging and downregulated by CR in more than 30 cell types (Figure 5C and Table S3). *Ybx1* was downregulated in more than 30 cell types during aging and upregulated by CR in more than 20 cell types, including ASCs in WAT (Figures 5C and S5A and Table S3). To investigate the role of *Ybx1* in the regulation of cellular homeostasis, we knocked down *Ybx1* in rat and human WAT ASCs, which resulted in progressive loss of cell proliferative potential, consistent with the exhaustion of this type of stem cells *in vivo* (Figures S5B–S5E). To explore the role of *Ybx1* in ASC maintenance, we performed bulk RNA-seq with *Ybx1*-knockdown samples (Figures S5F–S5J and Table S2). GO analysis revealed that the downregulated genes were primarily enriched in terms related to cell division and DNA replication (Figure S5H), consistent with the observed loss of cell proliferative potential upon *Ybx1* knockdown (Figures S5C–S5E). In addition, the upregulated genes were associated with chemotaxis and cytokine secretion (Figure S5G), consistent with the observed upregulation of the expression of a subset of SASP factors, including *Il1b*, due to *Ybx1* deficiency (Figure S5J). These data suggest that *Ybx1* may function as a key molecular switch between the effects of aging and CR, at least in ASCs.

Next, we sought to determine whether canonical aging hallmarks and nutrient-sensing pathways were regulated by aging and CR in a cell-type-specific manner at the single-cell level (Figures S5K–S5M). Classical aging-promoting genes and SASP genes (*Nfkb1a*, *Il6* and *Il1b*) were upregulated in most tissues and cell types and were partially suppressed by CR (Figures S5K and S5L and Table S2). Consistent with the functions of CR in modulating nutrient sensing, extracellular structure and growth factor pathways, the rescue DEGs included genes involved in AMPK, mTOR, insulin-like signaling (ILS), peroxisome proliferator-activated receptor gamma (PPAR- $\gamma$ ), and extracellular structure organization and cellular response to growth factor stimulus pathways (Figures S5M and S5N). Taken together,

these results provide a global assessment of aging and CR in rodents at the single-cell level and underscore the utility of large-scale, parallel gene expression analyses for studying complex biological phenomena.

### Reconstruction of Transcriptional Regulatory Networks by CR

To understand the transcriptional regulatory networks underlying aging and CR, we used SCENIC to predict the core transcription factors regulating aging and CR DEGs in the seven tissues (Figures 6A and 6B and Table S4). Transcription factors dysregulated during aging and restored by CR that were denoted as rescue transcription factors were distributed in the BAT, WAT, kidney, aortic, liver, and skin tissues (Figures 6C–6F). More than five rescue transcription factors were identified in the WAT (*Nfkb1*, *Rel*, *Cebpd*, *Atf3*, *Fos*, *Junb*, and *Mafb*), skin (*Cebpd*, *Cebpb*, *Atf3*, *Fos*, *Prnp*, and *Jun*), and kidney (*Cebpb*, *Cebpd*, *Foxi1*, *Mafb*, and *Myc*) (Figures 6E and 6F). Although the rescue transcription factors affected by CR were largely tissue specific, *Cebpd*, a leucine zipper transcription factor involved in inflammation and adipogenesis (Guo et al., 2015), was commonly downregulated during aging and upregulated by CR in BAT, WAT, and skin. Moreover, another leucine zipper transcription factor, *Cebpb*, which regulates genes involved in inflammatory responses, adipogenesis and tissue regeneration (Haase, 2015), was commonly downregulated during aging and upregulated by CR in the skin, aorta, and liver (Figures 6D and 6F). Along with aging-related downregulation of *Cebpd* and *Cebpb*, two central transcription factors in the activation of inflammation (Glass and Olefsky, 2012), *Nfkb1* and *Rel*, were upregulated during aging and downregulated by CR in WAT (Figures 6C and 6E). Taken together, these data reveal that CR reprograms the aging-compromised transcriptional regulatory networks and that transcription factors involved in inflammation and lipid metabolism may be interregulated by aging and CR.

### Erasure of Aging-Related Aberrant Cell-Cell Communication Patterns upon CR as Indicated by Computational Prediction

Altered intercellular communication is an integrative hallmark of aging (López-Otín et al., 2013). To investigate the redistribution of each kind of ligand-receptor interaction during aging and upon CR, we calculated the numbers of ligand-receptor pairs in every pair of cell types as well as during autocrine signaling in the same cell type in Y-AL, O-AL, and O-CR tissues. In total, we identified 456 kinds of potential ligand-receptor interaction pairs across different cell types in the seven tissues (Table S5). As shown in the cell-cell communication networks delineated by computational analysis (Figure 7A), cell-cell communication was enhanced in most O-AL tissues compared with Y-AL

#### Figure 4. CR as an Effective Intervention to Reprogram the Aging Transcriptome

(A) Venn diagrams showing the numbers of aging, CR, and rescue DEGs. The overlapping regions indicate the numbers of downregulated rescue DEGs (top) and upregulated rescue DEGs (bottom).

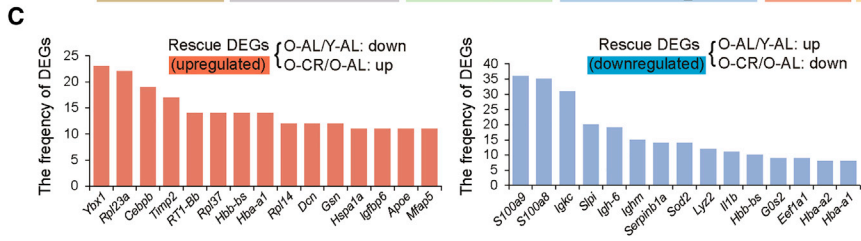
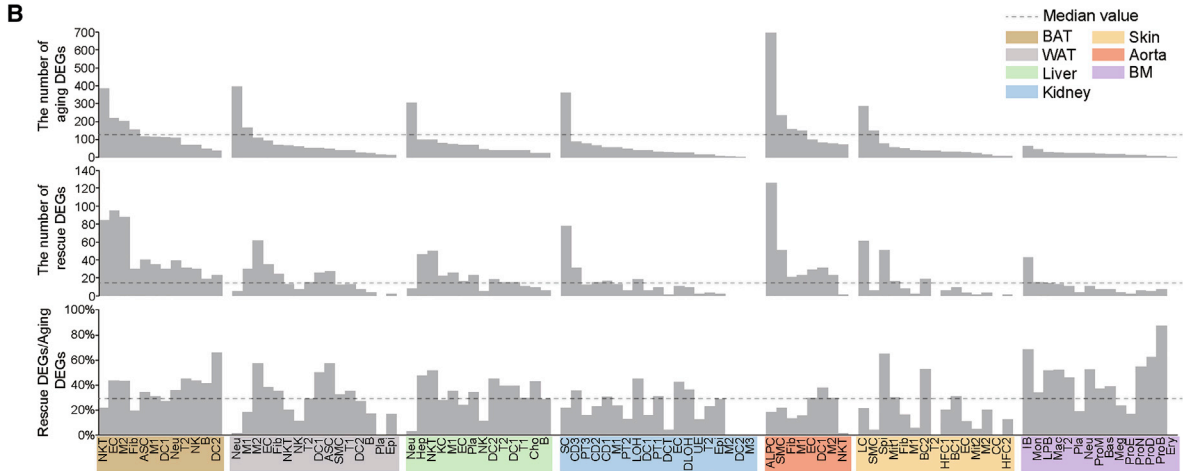
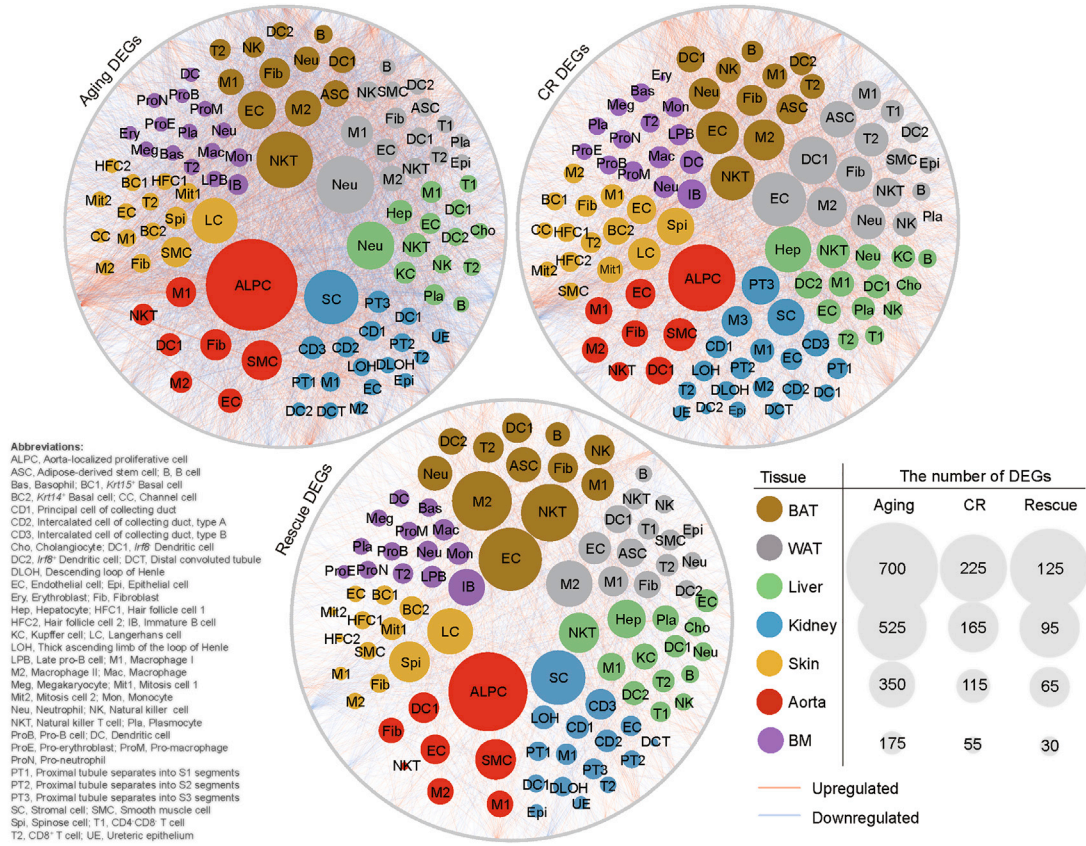
(B) Rose diagrams showing the numbers of aging DEGs, CR DEGs, and rescue DEGs in the seven tissues.

(C) Representative GO terms and pathways enriched in rescue DEGs based on functional enrichment analysis ( $p < 0.01$ ).

(D) Venn diagrams showing the numbers of upregulated and downregulated rescue DEGs in each tissue. The genes present in more than three types of tissues are labeled in the diagrams. The bold lines indicate the genes upregulated and downregulated in at least five tissues.

See also Figure S4 and Table S3.

**A** Cell-DEG networks



(legend on next page)

tissues. Conversely, many types of cell-cell communication between specific cell types in O-AL tissues were abolished by CR, especially in BAT, BM, kidney tissue, and liver tissue (Figure 7A). Specifically, ECs were pervasive in multiple tissues, and their interactions with other cell types were prevalently increased during aging and repressed upon CR, implying that ECs may serve as a common cell type for targeted aging intervention mediated by CR.

To identify the functions of ligand-receptor interactions affected during aging and CR, we performed GO and pathway enrichment analyses on the erased interactions, defined as the intercellular interactions present only in the O-AL group but not in the Y-AL or O-CR groups. Consistent with the aforementioned robust immunomodulatory function of CR, most of the erased interactions occurred between cytokines and cytokine receptors (Figure 7B). For example, TNFSF13B and TNFSF13 are two highly homologous cytokines that belong to the TNF ligand superfamily and serve as key plasmacyte survival factors (Tangye, 2011). Their interaction with the receptor TNFRSF13B was increased during aging and abolished by CR in tissues, including WAT, kidney tissue, and aortic tissue, in parallel with the changes in plasmacyte frequency in these tissues (Figure 7C). In addition, the interactions of ligand-receptor pairs such as IL17A-IL17 receptor AC, which induces neutrophil recruitment and inflammation (Gu et al., 2013), CD86-CD28, which primes T cells (Levine et al., 1995), and CSF3-CSF3R, which regulates granulopoiesis during inflammation, were abolished by CR in multiple tissues (Figure 7C) (Pazhakh et al., 2017). Herein, abnormal cell-cell communication patterns during aging, especially those that mediate inflammatory responses, were mitigated by CR.

### Sex-Dimorphic Changes in the Cell Type Composition and Transcriptional Profiles during Aging and CR

Next, we compared the data between male and female animals to determine whether sex dimorphism existed in the responses to aging and CR at the single-cell transcriptomic level. In general, no significant difference was detected in the disruption of the cell type composition by aging, the number of aging DEGs and the corresponding GO terms (Figures S6A–S6C). Accumulation of immune cells, especially neutrophils, was found in rats of both sexes during aging (Figures S6D–S6F). However, we observed sex-dimorphic sensitivity in the tissue-specific transcriptomic response to aging, as evidenced by the higher sensitivity of BAT to aging in males and that of the aorta to aging in females (Figure S6G). By comparison, CR alleviated aging-related accumulation of immune cells in rats of both sexes. In addition, the changes in the single-cell transcriptomic landscapes during aging were partially rescued by CR, with the most strongly enriched genes implicated in the inflammatory response in both male and

female rats (Figure S6C). However, the ratio of rescue DEGs to aging DEGs was higher in male rats than in female rats, suggesting that CR has a more prominent effect on aging in male rats (Figure S6B) (Anisimov et al., 2010). Thus, our work illustrates a multidimensional atlas of rodent single-cell transcriptomics with which to study the effects of aging and CR considering sex-specific effects, thus providing a comprehensive and valuable resource to the aging and metabolism fields.

### Single-Nucleus Transcriptomic Profiling of Brain and Skeletal Muscle Cells upon Aging and CR

Brain and skeletal muscle (SM) are two critical tissues that are affected by both aging and CR (López-Lluch and Navas, 2016). However, isolating viable intact single neurons or skeletal muscle cells from adult animals is very difficult (Lake et al., 2016). To broaden the scope of and add complexity to our aging and CR atlas, we circumvented this issue by single-nucleus RNA sequencing (snRNA-seq) (Lake et al., 2016) (Figure S7). After quality control, including doublet removal, we obtained 25,021 and 28,131 nuclei from the brain and skeletal muscle, respectively, from three groups of animals (Figures S7A and S7B and Table S1). From these datasets, we identified 10 major cell types in brain tissue and 11 major cell types in skeletal muscle (Figure S7C), all of which expressed annotated classical marker genes (Figures S7D and S7E).

We then examined the cell type compositional diversity in brain tissue and skeletal muscle during aging and CR. Similar to the observations in BAT and liver tissue, the numbers of ECs were decreased in both aged brain tissue and skeletal muscle and were partially restored in brain tissue from O-CR rats (Figure S7E). In addition, the percentage of inhibitory neurons was reduced during aging and restored upon CR (Figure S7E), consistent with the age-related synaptic changes in the inhibitory neurons in the human brain (Oh et al., 2016). However, the number of satellite cells was decreased in aged skeletal muscle compared to its young counterpart tissue but was not restored by CR (Figure S7E). In our attempt to identify aging DEGs, CR DEGs, and rescue DEGs using the snRNA-seq datasets, we found that the numbers of these DEGs in brain tissue and skeletal muscle were much lower than those revealed by scRNA-seq in the other tissues (except BM), possibly because of the differences in the abundance of nuclear RNA and cytosolic RNA (Lake et al., 2016). A total of 30 rescue DEGs were identified in skeletal muscle; approximately half were cytoskeletal genes, including *Tnnt1*, *Myh7*, and *Mylk2* (Figure S7F and Table S2). Of the 12 rescue DEGs in the brain, four genes (*Fanca*, *Ddit4*, *Spata22*, and *Msh3*) that were implicated in the cellular response to DNA damage were downregulated during aging and replenished upon CR (Figure S7F and Table S2). This portion of our study offers a transcriptomic view of the brain and skeletal

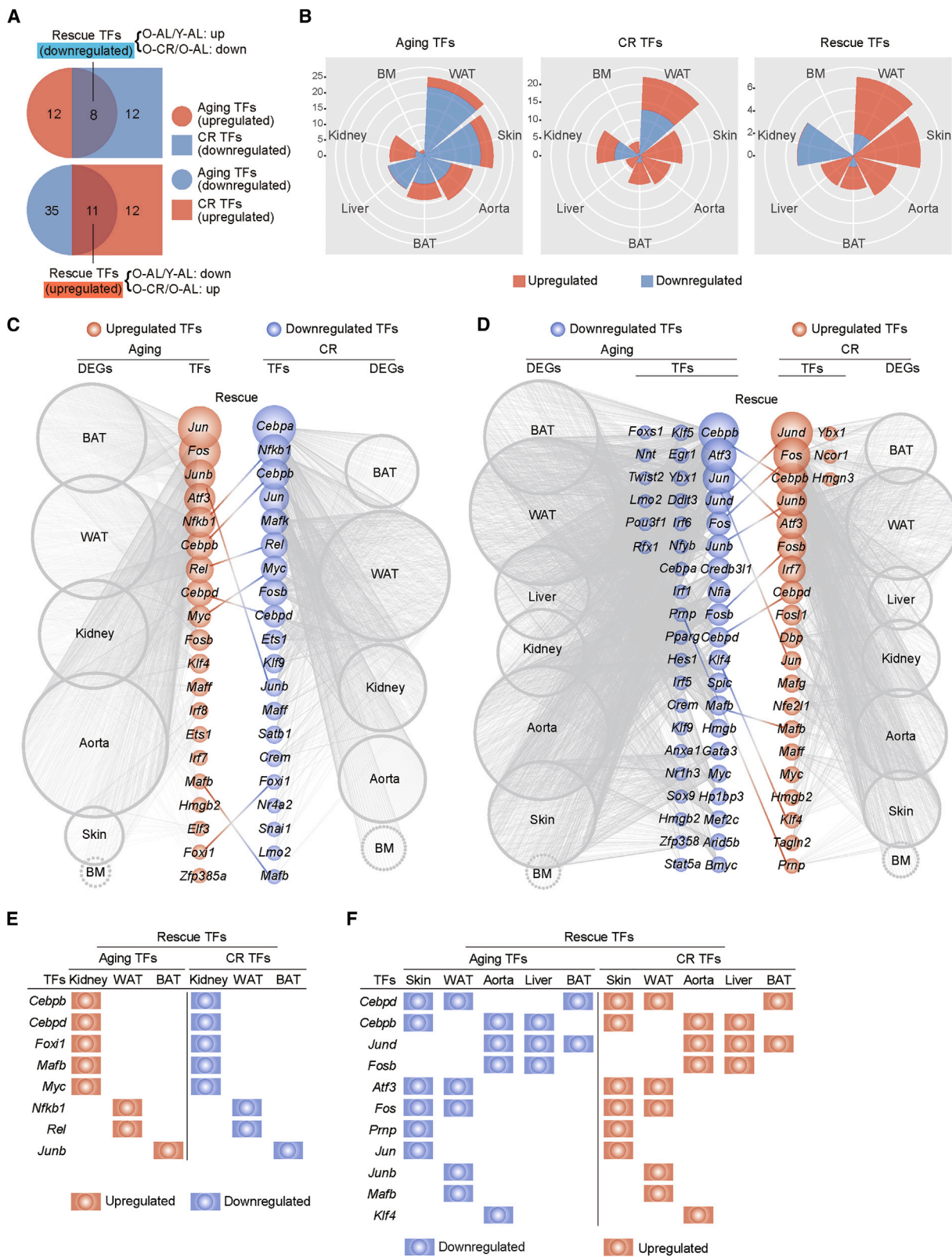
#### Figure 5. DEG Networks Resolving Gene Expression Heterogeneity among Different Cell Types

(A) Network plots showing the aging DEGs, CR DEGs, or rescue DEGs in each major cell type of all seven tissues. The internal nodes annotate cell types, and the different colors indicate different tissues. The gray circular edge denotes the collections of DEGs. Each cell type is connected with its DEGs by the internal lines of the network.

(B) Bar plots showing the numbers of aging and rescue DEGs and the percentages of rescue DEGs and aging DEGs in each cell type.

(C) Bar plots showing the frequencies of the top 15 rescue genes observed across all cell types in the seven tissues.

See also Figures S4, S5, and Table S2.



(legend on next page)

muscle of rats during aging and CR, providing a valuable source for gleaning additional information on the brain- and skeletal muscle-specific aging mechanisms and interventions.

## DISCUSSION

Here, we present a comprehensive single-cell compendium of the aging process in rats at the molecular level. We observed age-associated alterations in cell type composition, gene expression, transcriptional regulation, and cell-cell communication, which collectively provide insights into the mechanisms underlying aging. Moreover, we provide a single-cell analysis of animals subjected to CR during aging and unveil the mechanisms by which CR, as a powerful rejuvenation strategy, rescues many age-related phenotypic alterations. Together, our results identify a host of both age-associated and CR-rescued features at the molecular, cellular, tissue, and organismal levels, including cellular senescence, stem cell exhaustion, chronic inflammation, and aberrant cell-cell communications.

Several attempts have been made to identify the transcriptional changes during aging in individual cells and tissues, including human islets (Enge et al., 2017), monkey ovaries (Wang et al., 2020b), mouse T cells (Martinez-Jimenez et al., 2017), mouse lung tissues (Angelidis et al., 2019), mouse skin (Mahmoudi et al., 2019), mouse neural stem cells (Dulken et al., 2019), and *Drosophila* brain (Davie et al., 2018), at the single-cell level. Interestingly, increased numbers of immune cells, including eosinophils, T cells, and monocytes, were observed in aged lungs, along with increased levels of immunoglobulins and major histocompatibility complex (MHC) class I molecules as well as enhanced *Il6*, *Il8*, *Tnf*, and *Il1 $\gamma$*  signaling (Davie et al., 2018). Similarly, T cells with a high expression level of *Il1 $\gamma$*  have been found to infiltrate the neurogenic niches of aged mice, which may activate interferon signaling in nearby cells and thus reduce the number of neural stem cells (Dulken et al., 2019). These two studies and others support the idea that aging is closely associated with a proinflammatory state that contributes to the development of various chronic diseases (Dulken et al., 2019; Mahmoudi et al., 2019; Sarkar and Fisher, 2006).

The primary discovery in the current study is that the increase in the inflammatory response during aging could be systemically repressed by CR. Specifically, our data revealed that the number of plasmocytes, which are end-stage B lymphocytes, was increased in five types of tissues, including aortic tissue and BM, during aging and was suppressed in the aorta, liver, and WAT by CR. This finding is consistent with the previous result showing an increased number of plasmocytes in aged BM (Pioli et al., 2019). Additionally, neutrophils are a

crucial component of innate immunity derived from BM that are implicated in acute and chronic inflammation (Borregaard, 2010; Evrard et al., 2018; Jung et al., 2019). Neutrophils from aged mice show reduced apoptosis and an inaccurate migration ability, which may account for their retention in the lung parenchyma of aged mice (Jackaman et al., 2017). The results of these studies are consistent with our findings that aging is associated with increased neutrophil counts in multiple tissues, further pointing to the importance of unveiling the mechanism by which CR regulates neutrophils. M1/M2 macrophage activation is implicated in a wide range of aging-associated conditions, including obesity, atherosclerosis and hepatic fibrosis (Jackaman et al., 2017; Ma et al., 2018). Our results showed that macrophages were polarized toward a pro-inflammatory (M1) state during aging, while CR facilitated macrophage polarization toward an anti-inflammatory (M2) state with scavenger activity (Röszer, 2015). These changes in the immune cell type composition revealed a chronic inflammatory status in multiple aged tissues and indicated that this inflammation was repressed by CR. Consistent with our observation, three recently published studies revealed the drastic effects of CR on the number and localization of various immune cells (Buono and Longo, 2019; Collins et al., 2019; Jordan et al., 2019; Nagai et al., 2019). Notably, CR reduces the level of B cells in Peyer's patches (Nagai et al., 2019) and the number of circulating inflammatory monocytes by linking PPAR- $\gamma$  (or PPARG), a master regulator of lipid metabolism, to CCL2 production (Jordan et al., 2019). Thus, our study, along with previous reports, unveils the impact of CR on immunomodulation and emphasizes that metabolic interventions may affect the global immune response, which is strongly linked to the health status and lifespan of organisms.

Taken together, our results provide single-cell expression landmarks by which to systematically annotate rat cell types, identify sets of genes and key transcription factors differentially regulated during aging and CR, construct cell-cell communication networks modulated by aging and CR, and, overall, help elucidate the complex processes of aging and CR at single-cell resolution. Our study provides proof-of-concept by which single-cell atlases of multiple tissues may improve the understanding of the mechanisms underlying aging and metabolic intervention at a systemic level. In addition to the identification of aging and CR-associated transcriptomic changes in individual cells, the development of advanced single-cell measurement techniques for the simultaneous investigation of various changes in the epigenome, proteome, and posttranslational modifications, will enhance our knowledge of one of the most complex processes in biology, the aging of an organism, and ultimately,

### Figure 6. Changes in Core Regulatory Transcription Factors during Aging and CR

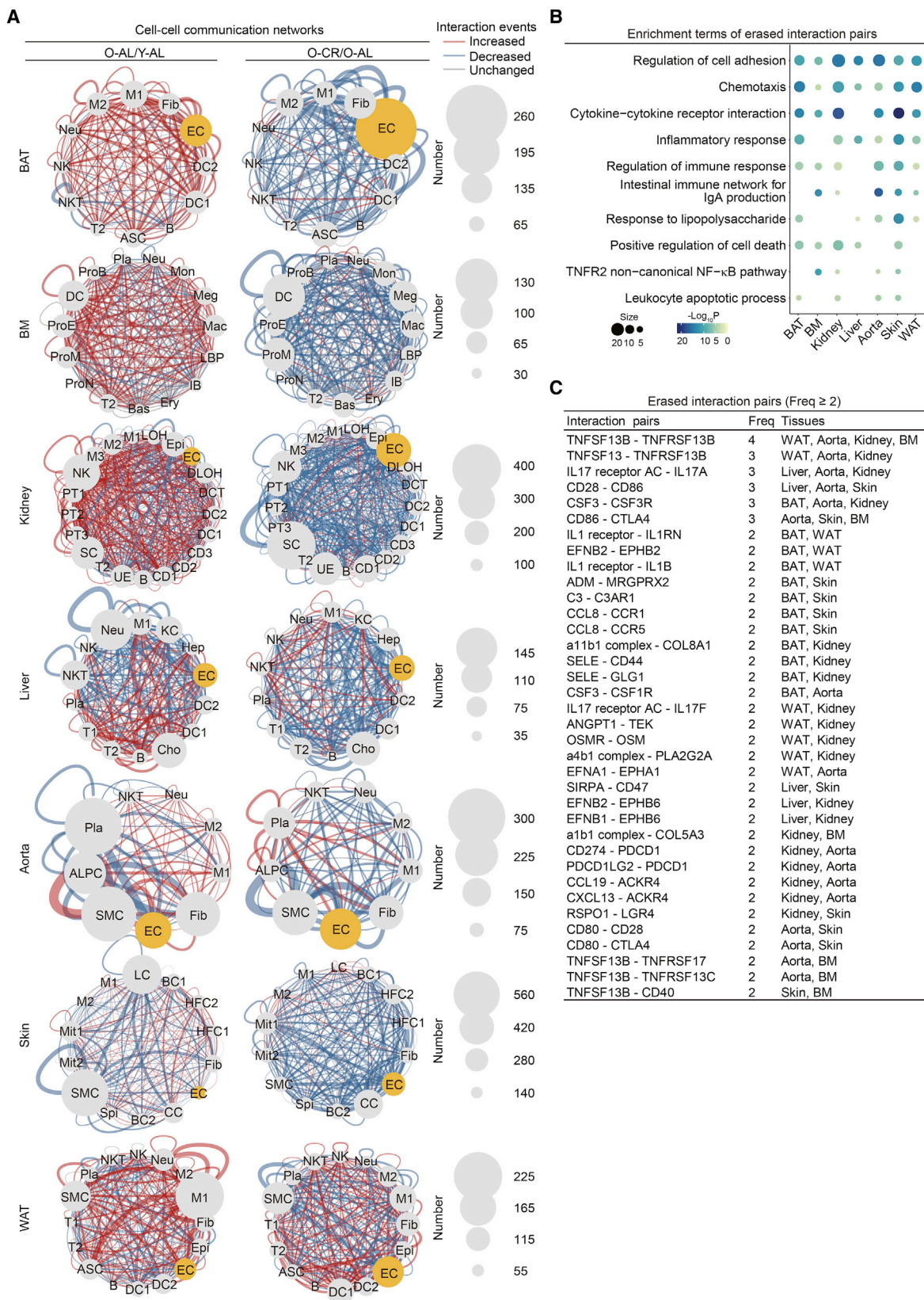
(A) Venn diagrams showing the numbers of aging, CR, and rescue TFs. The overlapping regions indicate the numbers of downregulated or upregulated rescue TFs.

(B) Rose diagrams showing the numbers of aging, CR, and rescue TFs in the seven tissues.

(C and D) Network visualization of potential downregulated (C) and upregulated (D) rescue TFs. The internal nodes annotate TFs; the gray circular edge denotes the downstream target DEGs of these TFs. The node sizes are positively correlated to the number of associated DEGs. The connecting line in the middle denotes rescue TFs.

(E and F) Downregulated (E) and upregulated (F) rescue TFs in the indicated tissues.

See also Table S4.



(legend on next page)

lead to the discovery of targets and strategies to increase life-span and healthspan.

## STAR★METHODS

Detailed methods are provided in the online version of this paper and include the following:

- **KEY RESOURCES TABLE**
- **LEAD CONTACT AND MATERIALS AVAILABILITY**
- **EXPERIMENTAL MODEL AND SUBJECT DETAILS**
  - Experimental animals
  - Human samples
- **METHOD DETAILS**
  - Rat strains and feeding plan
  - Tissue dissociation and cell isolation
  - Hematoxylin and eosin (H&E) staining
  - Masson's trichrome staining
  - SA- $\beta$ -Gal staining
  - Immunofluorescence microscopy
  - Western blotting
  - TUNEL staining
  - Oil Red O staining
  - Enzyme-linked immunosorbent assay (ELISA)
  - Flow cytometric analysis
  - Primary ASC culture
  - Analysis of cell cycle distribution
  - Clonal expansion assay
  - RNA interference and cell transfection
  - Nuclear isolation and snRNA-seq on the 10x genomics platform
  - Droplet-based scRNA-seq using the 10x genomics chromium platform
- **QUANTIFICATION AND STATISTICAL ANALYSIS**
  - Data processing
  - Clustering and identification of cell types
  - Cell type composition variation analysis
  - Pseudotime analysis
  - Differential expression and cell-DEG network analyses
  - GO analysis
  - Transcription factor-target gene network analysis
  - Cell-cell communication analysis
  - Bulk RNA-seq analysis
  - Statistical analysis
- **DATA AND CODE AVAILABILITY**

## SUPPLEMENTAL INFORMATION

Supplemental Information can be found online at <https://doi.org/10.1016/j.cell.2020.02.008>.

## ACKNOWLEDGMENTS

We thank Zhiheng He for his help in rat food intake. We thank Kai Du and Chunyu Chen from the Institute of Genetics and Developmental Biology, Chinese Academy of Sciences for their help in animal breeding. We thank Jinghui Lei and Jingyi Jia for assisting with animal experiments. We thank Yifang He, Yaobin Jing, Zunpeng Liu, Zehua Wang, Jinghui Lei, Xuling Han, Yiyuan Zhang, Guoxing Liu, Xing Zhang, Yaxin Wang, Jingyi Jia, Liyun Zhao, and Zeming Wu for participating in the single-cell isolation from specific rat tissues. We thank Yandong Zheng and Jiaming Li for bioinformatic analysis. We are also grateful to Lei Bai, Ruijun Bai, Jing Lu, Qun Chu, Ying Yang, May Schwarz, and Shikun Ma for administrative assistance, to Junying Jia from Institute of Biophysics, Chinese Academy of Sciences for the fluorescence-activated cell sorting (FACS), and to Junfeng Hao from Institute of Biophysics, Chinese Academy of Sciences for image scanning and analysis of Hematoxylin and eosin (H&E) staining. We would like to thank Hezhen Shan for her assistance with frozen tissue sections. We thank Prof. Zhengwei Xie for his advice on manuscript writing. This work was supported by the National Key Research and Development Program of China (2018YFC2000100), the Strategic Priority Research Program of the Chinese Academy of Sciences (XDA16010100), the National Key Research and Development Program of China (2018YFA0107203, 2017YFA0102802, 2017YFA0103304), the National Natural Science Foundation of China (81921006, 81625009, 91749202, 81861168034, 31671429, 91949209, 81671377, 91749123, 81771515, 31601158, 81701388, 81601233, 31601109, 81822018, 81870228, 81801399, 31801010, 81801370, 81922027, 31900523, 81901432, 81901433, 31900524), Program of Beijing Municipal Science and Technology Commission (Z191100001519005), Beijing Natural Science Foundation (Z190019), Beijing Municipal Commission of Health and Family Planning (PXM2018\_026283\_000002), Advanced Innovation Center for Human Brain Protection (3500-1192012), K.C. Wong Education Foundation (GJTD-2019-06, GJTD-2019-08), the Key Research Program of the Chinese Academy of Sciences (KFZD-SW-221), the State Key Laboratory of Stem Cell and Reproductive Biology, and the State Key Laboratory of Membrane Biology. J.C.I.B. was supported by the Moxie Foundation and the Glenn Foundation.

## AUTHOR CONTRIBUTIONS

G.-H.L., J.Q., W.Z., and J.C.I.B. conceptualized this project and supervised the overall experiments. S.M. performed bioinformatics analysis of the sc/snRNA-seq. L.G., S.S., W.W., Y.Y., Z.Z., W.L., and S.W. performed animal experiments and single-cell isolation of rat tissues. W.W. conducted the experiments of calorie restriction on rats. Q.J. performed bioinformatics analysis of bulk RNA-seq data. L.G. and Z.Z. performed immunostaining and tissue section analyses. Y.Y. performed FACS analyses. S.S. performed single nucleus isolation. X.L. provided human adipocyte tissues. G.-H.L., J.Q., W.Z., J.C.I.B., M.S., S.M., L.G., S.S., G.G., P.C., Q.Z., Y.Y., S.W., X.H., and C.R.E. performed manuscript writing, review, and editing.

## DECLARATION OF INTERESTS

The authors declare no competing interests.

Received: October 2, 2019

Revised: January 7, 2020

Accepted: February 4, 2020

Published: February 27, 2020

## Figure 7. Changes in Ligand-Receptor Interactions between Different Cell Types during Aging and CR

(A) Network plots showing the changes in ligand-receptor interaction events between different cell types in the O-AL/Y-AL and O-CR/O-AL comparison groups. Cell-cell communication is indicated by the connected line. The thickness of the lines is positively correlated with the number of ligand-receptor interaction events. The yellow node indicates ECs. Abbreviations for cell types are listed in Figure 5.

(B) Functional enrichment analysis showing the GO terms and pathways involving ligand-receptor interactions erased by CR. Erased terms are those present in the O-AL group and absent in the O-CR group ( $p < 0.01$ ).

(C) The frequency (Freq) of erased interaction pairs in the seven tissues (Freq  $\geq 2$ ).

See also Table S5.

## REFERENCES

- Ahmet, I., Tae, H.-J., de Cabo, R., Lakatta, E.G., and Talan, M.I. (2011). Effects of calorie restriction on cardioprotection and cardiovascular health. *J. Mol. Cell. Cardiol.* *51*, 263–271.
- Aibar, S., González-Blas, C.B., Moerman, T., Huynh-Thu, V.A., Imrichova, H., Hulselmans, G., Rambow, F., Marine, J.-C., Geurts, P., Aerts, J., et al. (2017). SCENIC: single-cell regulatory network inference and clustering. *Nat. Methods* *14*, 1083–1086.
- Angelidis, I., Simon, L.M., Fernandez, I.E., Strunz, M., Mayr, C.H., Greiffo, F.R., Tsitsiridis, G., Ansari, M., Graf, E., Strom, T.-M., et al. (2019). An atlas of the aging lung mapped by single cell transcriptomics and deep tissue proteomics. *Nat. Commun.* *10*, 963.
- Anisimov, V.N., Piskunova, T.S., Popovich, I.G., Zabezhinski, M.A., Tyndyk, M.L., Egorin, P.A., Yurova, M.V., Rosenfeld, S.V., Semenchenko, A.V., Kovalenko, I.G., et al. (2010). Gender differences in metformin effect on aging, life span and spontaneous tumorigenesis in 129/Sv mice. *Aging (Albany N.Y.)* *2*, 945–958.
- Bi, S., Wang, H., and Kuang, W. (2018). Stem cell rejuvenation and the role of autophagy in age retardation by caloric restriction: An update. *Mech. Ageing Dev.* *175*, 46–54.
- Borregaard, N. (2010). Neutrophils, from marrow to microbes. *Immunity* *33*, 657–670.
- Buono, R., and Longo, V.D. (2019). When Fasting Gets Tough, the Tough Immune Cells Get Going-or Die. *Cell* *178*, 1038–1040.
- Butler, A., Hoffman, P., Smibert, P., Papalexis, E., and Satija, R. (2018). Integrating single-cell transcriptomic data across different conditions, technologies, and species. *Nat. Biotechnol.* *36*, 411–420.
- Campisi, J., Kapahi, P., Lithgow, G.J., Melov, S., Newman, J.C., and Verdin, E. (2019). From discoveries in ageing research to therapeutics for healthy ageing. *Nature* *571*, 183–192.
- Cheng, F., Wang, S., Song, M., Liu, Z., Liu, P., Wang, L., Wang, Y., Zhao, Q., Yan, K., Chan, P., et al. (2019). DJ-1 is dispensable for human stem cell homeostasis. *Protein Cell* *10*, 846–853.
- Childs, B., and van Deursen, J. (2019). Inhibition of ‘jumping genes’ promotes healthy ageing. *Nature* *566*, 46–48.
- Collins, N., Han, S.-J., Enamorado, M., Link, V.M., Huang, B., Moseman, E.A., Kishton, R.J., Shannon, J.P., Dixit, D., Schwab, S.R., et al. (2019). The Bone Marrow Protects and Optimizes Immunological Memory during Dietary Restriction. *Cell* *178*, 1088–1101.e15.
- Contreras, N.A., Fontana, L., Tosti, V., and Nikolich-Zugich, J. (2018). Calorie restriction induces reversible lymphopenia and lymphoid organ atrophy due to cell redistribution. *Geroscience* *40*, 279–291.
- Davie, K., Janssens, J., Koldere, D., De Waegeneer, M., Pech, U., Kreft, Ł., Aibar, S., Makhzami, S., Christiaens, V., Bravo González-Blas, C., et al. (2018). A Single-Cell Transcriptome Atlas of the Aging Drosophila Brain. *Cell* *174*, 982–998.e20.
- Debacq-Chainiaux, F., Erusalimsky, J.D., Campisi, J., and Toussaint, O. (2009). Protocols to detect senescence-associated beta-galactosidase (SA-beta-gal) activity, a biomarker of senescent cells in culture and in vivo. *Nat. Protoc.* *4*, 1798–1806.
- Di Giammartino, D.C., Kloetgen, A., Polyzos, A., Liu, Y., Kim, D., Murphy, D., Abuhashem, A., Cavaliere, P., Aronson, B., Shah, V., et al. (2019). KLF4 is involved in the organization and regulation of pluripotency-associated three-dimensional enhancer networks. *Nat. Cell Biol.* *21*, 1179–1190.
- Dulken, B.W., Buckley, M.T., Navarro Negredo, P., Saligrama, N., Cayrol, R., Leeman, D.S., George, B.M., Boutet, S.C., Hebestreit, K., Pluvinau, J.V., et al. (2019). Single-cell analysis reveals T cell infiltration in old neurogenic niches. *Nature* *571*, 205–210.
- Enge, M., Arda, H.E., Mignardi, M., Beausang, J., Bottino, R., Kim, S.K., and Quake, S.R. (2017). Single-Cell Analysis of Human Pancreas Reveals Transcriptional Signatures of Aging and Somatic Mutation Patterns. *Cell* *171*, 321–330.e14.
- Evrard, M., Kwok, I.W.H., Chong, S.Z., Teng, K.W.W., Becht, E., Chen, J., Sieow, J.L., Penny, H.L., Ching, G.C., Devi, S., et al. (2018). Developmental Analysis of Bone Marrow Neutrophils Reveals Populations Specialized in Expansion, Trafficking, and Effector Functions. *Immunity* *48*, 364–379.e8.
- Fontana, L., and Partridge, L. (2015). Promoting health and longevity through diet: from model organisms to humans. *Cell* *161*, 106–118.
- Forni, M.F., Peggion, J., Braga, T.T., Chinchilla, J.E.O., Shinohara, J., Navas, C.A., Camara, N.O.S., and Kowaltowski, A.J. (2017). Caloric restriction promotes structural and metabolic changes in the skin. *Cell Rep.* *20*, 2678–2692.
- Fujii, N., Uta, S., Kobayashi, M., Sato, T., Okita, N., and Higami, Y. (2019). Impact of aging and caloric restriction on fibroblast growth factor 21 signaling in rat white adipose tissue. *Exp. Gerontol.* *118*, 55–64.
- Geng, L., Liu, Z., Wang, S., Sun, S., Ma, S., Liu, X., Chan, P., Sun, L., Song, M., Zhang, W., et al. (2019). Low-dose quercetin positively regulates mouse healthspan. *Protein Cell* *10*, 770–775.
- Glass, C.K., and Olefsky, J.M. (2012). Inflammation and lipid signaling in the etiology of insulin resistance. *Cell Metab.* *15*, 635–645.
- Griffiths, J.A., Richard, A.C., Bach, K., Lun, A.T.L., and Marioni, J.C. (2018). Detection and removal of barcode swapping in single-cell RNA-seq data. *Nat. Commun.* *9*, 2667.
- Gu, C., Wu, L., and Li, X. (2013). IL-17 family: cytokines, receptors and signaling. *Cytokine* *64*, 477–485.
- Guo, L., Li, X., and Tang, Q.-Q. (2015). Transcriptional regulation of adipocyte differentiation: a central role for CCAAT/enhancer-binding protein (C/EBP)  $\beta$ . *J. Biol. Chem.* *290*, 755–761.
- Haase, V.H. (2015). Inflammation and hypoxia in the kidney: friends or foes? *Kidney Int.* *88*, 213–215.
- Han, X., Wang, R., Zhou, Y., Fei, L., Sun, H., Lai, S., Saadatpour, A., Zhou, Z., Chen, H., Ye, F., et al. (2018). Mapping the Mouse Cell Atlas by Microwell-Seq. *Cell* *172*, 1091–1107.e17.
- Huynh-Thu, V.A., Irrthum, A., Wehenkel, L., and Geurts, P. (2010). Inferring regulatory networks from expression data using tree-based methods. *PLoS ONE* *5*, e12776.
- Jackaman, C., Tomay, F., Duong, L., Abdol Razak, N.B., Pixley, F.J., Metharom, P., and Nelson, D.J. (2017). Aging and cancer: The role of macrophages and neutrophils. *Ageing Res. Rev.* *36*, 105–116.
- Jordan, S., Tung, N., Casanova-Acebes, M., Chang, C., Cantoni, C., Zhang, D., Wirtz, T.H., Naik, S., Rose, S.A., Brocker, C.N., et al. (2019). Dietary Intake Regulates the Circulating Inflammatory Monocyte Pool. *Cell* *178*, 1102–1114.e17.
- Jung, N., Bueb, J.L., Tolle, F., and Bréchard, S. (2019). Regulation of neutrophil pro-inflammatory functions sheds new light on the pathogenesis of rheumatoid arthritis. *Biochem. Pharmacol.* *165*, 170–180.
- Kharitonov, A., Shiyanova, T.L., Koester, A., Ford, A.M., Micanovic, R., Galbreath, E.J., Sandusky, G.E., Hammond, L.J., Moyers, J.S., Owens, R.A., et al. (2005). FGF-21 as a novel metabolic regulator. *J. Clin. Invest.* *115*, 1627–1635.
- Kim, D., Langmead, B., and Salzberg, S.L. (2015). HISAT: a fast spliced aligner with low memory requirements. *Nat. Methods* *12*, 357–360.
- Kretov, D.A., Clément, M.-J., Lambert, G., Durand, D., Lyabin, D.N., Bollot, G., Bauvais, C., Samsonova, A., Budkina, K., Maroun, R.C., et al. (2019). YB-1, an abundant core mRNA-binding protein, has the capacity to form an RNA nucleoprotein filament: a structural analysis. *Nucleic Acids Res.* *47*, 3127–3141.
- Krishnaswami, S.R., Grindberg, R.V., Novotny, M., Venepally, P., Lacar, B., Bhutani, K., Linker, S.B., Pham, S., Erwin, J.A., Miller, J.A., et al. (2016). Using single nuclei for RNA-seq to capture the transcriptome of postmortem neurons. *Nat. Protoc.* *11*, 499–524.
- Lake, B.B., Ai, R., Kaeser, G.E., Salathia, N.S., Yung, Y.C., Liu, R., Wildberg, A., Gao, D., Fung, H.-L., Chen, S., et al. (2016). Neuronal subtypes and diversity revealed by single-nucleus RNA sequencing of the human brain. *Science* *352*, 1586–1590.

- Levay, E.A., Govic, A., Penman, J., Paolini, A.G., and Kent, S. (2007). Effects of adult-onset calorie restriction on anxiety-like behavior in rats. *Physiol. Behav.* **92**, 889–896.
- Levine, B.L., Ueda, Y., Craighead, N., Huang, M.L., and June, C.H. (1995). CD28 ligands CD80 (B7-1) and CD86 (B7-2) induce long-term autocrine growth of CD4+ T cells and induce similar patterns of cytokine secretion *in vitro*. *Int. Immunol.* **7**, 891–904.
- Liao, Y., Smyth, G.K., and Shi, W. (2014). featureCounts: an efficient general purpose program for assigning sequence reads to genomic features. *Bioinformatics* **30**, 923–930.
- Liu, Y.-C., Zou, X.-B., Chai, Y.-F., and Yao, Y.-M. (2014). Macrophage polarization in inflammatory diseases. *Int. J. Biol. Sci.* **10**, 520–529.
- Lomako, V.V., and Shylo, O.V. (2019). [Transformation of erythrocytes in rats of different ages]. *Adv. Gerontol.* **9**, 298–302.
- López-Lluch, G., and Navas, P. (2016). Calorie restriction as an intervention in ageing. *J. Physiol.* **594**, 2043–2060.
- López-Otín, C., Blasco, M.A., Partridge, L., Serrano, M., and Kroemer, G. (2013). The hallmarks of aging. *Cell* **153**, 1194–1217.
- Love, M.I., Huber, W., and Anders, S. (2014). Moderated estimation of fold change and dispersion for RNA-seq data with DESeq2. *Genome Biol.* **15**, 550.
- Ma, Y., Mouton, A.J., and Lindsey, M.L. (2018). Cardiac macrophage biology in the steady-state heart, the aging heart, and following myocardial infarction. *Transl. Res.* **197**, 15–28.
- Macosko, E.Z., Basu, A., Satija, R., Nemes, J., Shekhar, K., Goldman, M., Tirosh, I., Bialas, A.R., Kamitaki, N., Martersteck, E.M., et al. (2015). Highly parallel genome-wide expression profiling of individual cells using nanoliter droplets. *Cell* **161**, 1202–1214.
- Mahmoudi, S., Mancini, E., Xu, L., Moore, A., Jahanbani, F., Hebestreit, K., Srinivasan, R., Li, X., Devarajan, K., Prélôt, L., et al. (2019). Heterogeneity in old fibroblasts is linked to variability in reprogramming and wound healing. *Nature* **574**, 553–558.
- Martinez-Jimenez, C.P., Eling, N., Chen, H.-C., Vallejos, C.A., Kolodziejczyk, A.A., Connor, F., Stojic, L., Rayner, T.F., Stubbington, M.J.T., Teichmann, S.A., et al. (2017). Aging increases cell-to-cell transcriptional variability upon immune stimulation. *Science* **355**, 1433–1436.
- McCay, C.M., Crowell, M.F., and Maynard, L.A. (1935). The effect of retarded growth upon the length of life span and upon the ultimate body size. *J. Nutr.* **10**, 63–79.
- McGinnis, Christopher S., LyndsayMorrow, M., and Zev, J.G. (2019). Doublet-Finder: Doublet detection in single-cell RNA sequencing data using artificial nearest neighbors. *Cell systems* **8**, 329–337.
- Ménard, C., Quirion, R., Bouchard, S., Ferland, G., and Gaudreau, P. (2014). Glutamatergic signaling and low prodynorphin expression are associated with intact memory and reduced anxiety in rat models of healthy aging. *Front. Aging Neurosci.* **6**, 81.
- Nagai, M., Noguchi, R., Takahashi, D., Morikawa, T., Koshida, K., Komiyama, S., Ishihara, N., Yamada, T., Kawamura, Y.I., Muroi, K., et al. (2019). Fasting-Refeeding Impacts Immune Cell Dynamics and Mucosal Immune Responses. *Cell* **178**, 1072–1087.e14.
- Niederberger, C., Pellicer, A., Cohen, J., Gardner, D.K., Palermo, G.D., O'Neill, C.L., Chow, S., Rosenwaks, Z., Cobo, A., Swain, J.E., et al. (2018). Forty years of IVF. *Fertil. Steril.* **110**, 185–324.e5.
- Oh, H., Lewis, D.A., and Sibille, E. (2016). The Role of BDNF in Age-Dependent Changes of Excitatory and Inhibitory Synaptic Markers in the Human Prefrontal Cortex. *Neuropsychopharmacology* **41**, 3080–3091.
- Papalex, E., and Satija, R. (2018). Single-cell RNA sequencing to explore immune cell heterogeneity. *Nat. Rev. Immunol.* **18**, 35–45.
- Pazhakh, V., Clark, S., Keightley, M.C., and Lieschke, G.J. (2017). A GCSFR/CSF3R zebrafish mutant models the persistent basal neutrophil deficiency of severe congenital neutropenia. *Sci. Rep.* **7**, 44455.
- Pifferi, F., and Aujard, F. (2019). Caloric restriction, longevity and aging: Recent contributions from human and non-human primate studies. *Prog. Neuropsychopharmacol. Biol. Psychiatry* **95**, 109702.
- Pioli, P.D., Casero, D., Montecino-Rodriguez, E., Morrison, S.L., and Dorshkind, K. (2019). Plasma Cells Are Obligate Effectors of Enhanced Myelopoiesis in Aging Bone Marrow. *Immunity* **51**, 351–366.e6.
- Qiu, X., Mao, Q., Tang, Y., Wang, L., Chawla, R., Pliner, H.A., and Trapnell, C. (2017). Reversed graph embedding resolves complex single-cell trajectories. *Nat. Methods* **14**, 979–982.
- Reckless, J., Tatalick, L.M., and Grainger, D.J. (2001). The pan-chemokine inhibitor NR58-3.14.3 abolishes tumour necrosis factor- $\alpha$  accumulation and leucocyte recruitment induced by lipopolysaccharide *in vivo*. *Immunology* **103**, 244–254.
- Redman, L.M., Smith, S.R., Burton, J.H., Martin, C.K., Il'yasova, D., and Ravussin, E. (2018). Metabolic slowing and reduced oxidative damage with sustained caloric restriction support the rate of living and oxidative damage theories of aging. *Cell Metab.* **27**, 805–815.e4.
- Rhoads, T.W., Burhans, M.S., Chen, V.B., Hutchins, P.D., Rush, M.J.P., Clark, J.P., Stark, J.L., McIlwain, S.J., Eghbalian, H.R., Pavelec, D.M., et al. (2018). Caloric restriction engages hepatic RNA processing mechanisms in rhesus monkeys. *Cell Metab.* **27**, 677–688.e5.
- Rojek, A., Fuchtbauer, E.-M., Fuchtbauer, A., Jelen, S., Malmendal, A., Fenton, R.A., and Nielsen, S. (2013). Liver-specific Aquaporin 11 knockout mice show rapid vacuolization of the rough endoplasmic reticulum in periportal hepatocytes after amino acid feeding. *Am. J. Physiol. Gastrointest. Liver Physiol.* **304**, G501–G515.
- Röszer, T. (2015). Understanding the mysterious M2 macrophage through activation markers and effector mechanisms. *Mediators Inflamm.* **2015**, 816460.
- Sarkar, D., and Fisher, P.B. (2006). Molecular mechanisms of aging-associated inflammation. *Cancer Lett.* **236**, 13–23.
- Schaum, N., Karkanas, J., Neff, N.F., May, A.P., Quake, S.R., Wyss-Coray, T., Darmanis, S., Batson, J., Botvinnik, O., Chen, M.B., et al.; Tabula Muris Consortium; Overall coordination; Logistical coordination; Organ collection and processing; Library preparation and sequencing; Computational data analysis; Cell type annotation; Writing group; Supplemental text writing group; Principal investigators (2018). Single-cell transcriptomics of 20 mouse organs creates a Tabula Muris. *Nature* **562**, 367–372.
- Shannon, P., Markiel, A., Ozier, O., Baliga, N.S., Wang, J.T., Ramage, D., Amin, N., Schwikowski, B., and Ideker, T. (2003). Cytoscape: a software environment for integrated models of biomolecular interaction networks. *Genome Res.* **13**, 2498–2504.
- Spindler, S.R. (2010). Caloric restriction: from soup to nuts. *Ageing Res. Rev.* **9**, 324–353.
- Talukdar, S., Oh, D.Y., Bandyopadhyay, G., Li, D., Xu, J., McNelis, J., Lu, M., Li, P., Yan, Q., Zhu, Y., et al. (2012). Neutrophils mediate insulin resistance in mice fed a high-fat diet through secreted elastase. *Nat. Med.* **18**, 1407–1412.
- Tang, F., Barbacioru, C., Wang, Y., Nordman, E., Lee, C., Xu, N., Wang, X., Bodeau, J., Tuch, B.B., Siddiqui, A., et al. (2009). mRNA-Seq whole-transcriptome analysis of a single cell. *Nat. Methods* **6**, 377–382.
- Tangye, S.G. (2011). Staying alive: regulation of plasma cell survival. *Trends Immunol.* **32**, 595–602.
- Trim, W., Turner, J.E., and Thompson, D. (2018). Parallels in immunometabolic adipose tissue dysfunction with ageing and obesity. *Front. Immunol.* **9**, 169.
- Vento-Tormo, R., Efremova, M., Botting, R.A., Turco, M.Y., Vento-Tormo, M., Meyer, K.B., Park, J.-E., Stephenson, E., Polański, K., Goncalves, A., et al. (2018). Single-cell reconstruction of the early maternal-fetal interface in humans. *Nature* **563**, 347–353.
- Verfaillie, A., Imrichova, H., Janky, R., and Aerts, S. (2015). iRegulon and i-cis-Target: reconstructing regulatory networks using motif and track enrichment. *Curr. Protoc. Bioinformatics* **52**, 1–39.
- Wang, S., Min, Z., Ji, Q., Geng, L., Su, Y., Liu, Z., Hu, H., Wang, L., Zhang, W., Suzuki, K., et al. (2020a). Rescue of premature aging defects in Cockayne

syndrome stem cells by CRISPR/Cas9-mediated gene correction. *Protein Cell* *11*, 1–22.

Wang, S., Zheng, X., Li, J., Yu, Y., Zhang, W., Belmonte, J.C.I., Qu, J., Tang, F., and Liu, G.-H. (2020b). Single-Cell Transcriptomic Atlas of Primate Ovarian Aging (CELL) <https://doi.org/10.1016/j.cell.2020.01.009>.

Wang, Z., He, Y., Deng, W., Lang, L., Yang, H., Jin, B., Kolhe, R., Ding, H.F., Zhang, J., Hai, T., and Yan, C. (2018). Atf3 deficiency promotes genome instability and spontaneous tumorigenesis in mice. *Oncogene* *37*, 18–27.

Wasinski, F., Bacurau, R.F.P., Moraes, M.R., Haro, A.S., Moraes-Vieira, P.M.M., Estrela, G.R., Paredes-Gamero, E.J., Barros, C.C., Almeida, S.S., Câmara, N.O.S., and Araujo, R.C. (2013). Exercise and caloric restriction alter the immune system of mice submitted to a high-fat diet. *Mediators Inflamm.* *2013*, 395672.

Wickham, H. (2016). *ggplot2: Elegant Graphics for Data Analysis* (Springer Publishing Company, Incorporated).

Wood, S.H., van Dam, S., Craig, T., Tacutu, R., O'Toole, A., Merry, B.J., and de Magalhães, J.P. (2015). Transcriptome analysis in calorie-restricted rats implicates epigenetic and post-translational mechanisms in neuroprotection and aging. *Genome Biol.* *16*, 285.

Zhang, R., Chen, H.-Z., and Liu, D.-P. (2015). The four layers of aging. *Cell Syst.* *1*, 180–186.

Zhang, W., Qu, J., Liu, G.-H., and Belmonte, J.C.I. (2020). The ageing epigenome and its rejuvenation. *Nat. Rev. Mol. Cell Biol.* <https://doi.org/10.1038/s41580-019-0204-5>.

Zhou, Y., Zhou, B., Pache, L., Chang, M., Khodabakhshi, A.H., Tanaseichuk, O., Benner, C., and Chanda, S.K. (2019). Metascape provides a biologist-oriented resource for the analysis of systems-level datasets. *Nat. Commun.* *10*, 1523.

Zou, K., Ouyang, Q., Li, H., and Zheng, J. (2017). A global characterization of the translational and transcriptional programs induced by methionine restriction through ribosome profiling and RNA-seq. *BMC Genomics* *18*, 189.

## STAR★METHODS

## KEY RESOURCES TABLE

REAGENT or RESOURCE	SOURCE	IDENTIFIER
<b>Antibodies</b>		
anti-CD68	Abcam	Cat# ab125212; RRID: AB_10975465
anti-syndecan-1 (CD138)	Abcam	Cat# ab34164; RRID: AB_778207
anti-Granulocytes (Neutrophil)	Abcam	Cat# ab33760; RRID: AB_732699
anti-SMA	Zsbio	Cat# ZM0003
anti-Ki67	Zsbio	Cat# ZM0166
anti-LINE1-ORF1p	Millipore	Cat# MABC1152
anti-GAPDH	Abcam	Cat# ab8245; RRID: AB_2107448
anti-YBX1	Abcam	Cat# ab12148; RRID: AB_2219278
anti-CD3-FITC	BD Biosciences	Cat# 559975; RRID: AB_397402
anti-CD8-Alexa Fluor® 647	BD Biosciences	Cat# 561611; RRID: AB_10893006
<b>Experimental Models: Cell Lines</b>		
Human primary ASCs from WAT of a 24-year-old woman	This study	N/A
Rat primary ASCs from female rat WAT	This study	N/A
HEK293T cells	ATCC	Cat# CRL-1573; RRID: CVCL_0045
<b>Chemicals, Peptides, and Recombinant Proteins</b>		
Lipofectamine 3000 Reagent	Thermo Fisher Scientific	Cat# L3000015
DMEM/F12 Medium	Thermo Fisher Scientific	Cat# 11320-033
FBS	GIBCO	Cat# 10270-106; LOT# 42F9083K
Collagenase I	GIBCO	Cat# 17100017
Collagenase IV	GIBCO	Cat# 17104-019
0.25% Trypsin-EDTA	GIBCO	Cat# 25200-072
Dispase	GIBCO	Cat# 17105041
Collagenase II	GIBCO	Cat# 17101-015
Elastase	Sigma	Cat# E1250
Deoxyribonuclease I	Worthington	Cat# LS006333
RBC lysis buffer	BD Biosciences	Cat# 555899
7-Amino-Actinomycin D (7-AAD)	BD Biosciences	Cat# 559925
Crystal violet	Biohao Biotechnology, China	Cat# 0502
bFGF	Joint Protein Central	Cat# BBI-EXP-002
Oil Red O	Sigma-Aldrich	Cat# O0625
4% paraformaldehyde, PFA	Dingguo, China	Cat# AR-0211
Triton X-100	Sigma-Aldrich	Cat# T9284
RNaseIn	Thermo Fisher Scientific	Cat# AM2694
Supersasin	Promega	Cat# N2615
<b>Critical Commercial Assays</b>		
Chromium Single Cell 3' Library & Gel Bead Kit v2	10x Genomics	120237
Chromium Single Cell A Chip Kit	10x Genomics	120236
Chromium i7 Multiplex Kit	10x Genomics	120262
Rat S100 calcium binding protein A8 ELISA Kit	CUSABIO	Cat# CSB-EL020641RA
Rat tumor necrosis factor-(TNF $\alpha$ ) ELISA Kit	Thermo Fisher Scientific	Cat# 88-7340
<i>In Situ</i> Cell Death Detection Kit, POD	Roche	Cat# 11684817910

(Continued on next page)

**Continued**

REAGENT or RESOURCE	SOURCE	IDENTIFIER
Deposited Data		
Raw data files and processed data files for RNA-seq	This study	GEO: GSE137869
Recombinant DNA		
pLVTHM	A gift from Didier Trono	Addgene plasmid #12247
psPAX2	A gift from Didier Trono	Addgene plasmid #12260
pMD2.G	A gift from Didier Trono	Addgene plasmid #12259
Experimental Models: Organisms/Strains		
Human WAT	Peking Union Medical College Hospital	N/A
<i>Sprague Dawley</i> (SD) rats	Beijing Vital River Laboratory Animal Technology Co., Ltd., which is joint ventures of Charles River Laboratories in China	N/A
Oligonucleotides		
shYbx1-F:CGCGTGCCACGCAATTACCAGCAAA TTCAAGAGATTTGCTGGTAATTGCGTGGCTTTT TTGGAAT	Thermo Fisher Scientific	N/A
shYbx1-R:CGATTTCCAAAAAGCCACGCAATT ACCAGCAAATCTCTTGAATTTGCTGGTAATTG CGTGGCA	Thermo Fisher Scientific	N/A
Software and Algorithms		
bcl2fastq (version: 2.20.0.422)	Illumina	<a href="https://support.illumina.com/sequencing/sequencing_software/bcl2fastq-conversion-software.html">https://support.illumina.com/sequencing/sequencing_software/bcl2fastq-conversion-software.html</a>
Cell Ranger (version: 2.2.0)	10x Genomics	<a href="https://support.10xgenomics.com/single-cell-gene-expression/software/downloads/latest">https://support.10xgenomics.com/single-cell-gene-expression/software/downloads/latest</a>
Metascape (version: 3.5)	(Zhou et al., 2019)	<a href="http://metascape.org/">http://metascape.org/</a>
Seurat (version: 2.3.4)	(Butler et al., 2018)	<a href="https://satijalab.org/seurat/">https://satijalab.org/seurat/</a>
Image Lab (version: 4.0)	Bio-Rad	<a href="https://www.bio-rad.com/zh-cn/product/imagelab-software?ID=KRE6P5E8Z">https://www.bio-rad.com/zh-cn/product/imagelab-software?ID=KRE6P5E8Z</a>
ImageJ (version: 1.8.0)	NIH	<a href="https://imagej.nih.gov/ij/">https://imagej.nih.gov/ij/</a>
FlowJo (version: 10.0.7)	FlowJo, LLC	<a href="https://www.flowjo.com/">https://www.flowjo.com/</a>
Leica LAS AF Lite (version: 2.6.0)	Leica	<a href="https://leica-las-af-lite.updatestar.com/">https://leica-las-af-lite.updatestar.com/</a>
GraphPad Prism 6	GraphPad Software Inc.	<a href="https://www.graphpad.com/scientific-software/prism/">https://www.graphpad.com/scientific-software/prism/</a>
SCENIC (version: 1.1.2.2)	(Aibar et al., 2017)	<a href="https://github.com/aertslab/SCENIC">https://github.com/aertslab/SCENIC</a>
DoubletFinder (version: 2.0.2)	(McGinnis et al., 2019)	<a href="https://github.com/chris-mcginnis-ucsf/DoubletFinder">https://github.com/chris-mcginnis-ucsf/DoubletFinder</a>
Monocle (version: 2.6.4)	(Qiu et al., 2017)	<a href="http://cole-trapnell-lab.github.io/monocle-release/docs/">http://cole-trapnell-lab.github.io/monocle-release/docs/</a>
DropletUtils (version: 1.6.1)	(Griffiths et al., 2018)	<a href="http://bioconductor.org/packages/release/bioc/html/DropletUtils.html">http://bioconductor.org/packages/release/bioc/html/DropletUtils.html</a>
pheatmap (version: 1.0.12)	N/A	<a href="https://cran.r-project.org/web/packages/pheatmap/index.html">https://cran.r-project.org/web/packages/pheatmap/index.html</a>
ggplot2 (version: 3.2.1)	(Wickham, 2016)	<a href="https://ggplot2.tidyverse.org/">https://ggplot2.tidyverse.org/</a>
GENIE3 (version: 1.6.0)	(Huynh-Thu et al., 2010)	<a href="https://bioconductor.org/packages/release/bioc/html/GENIE3.html">https://bioconductor.org/packages/release/bioc/html/GENIE3.html</a>
Cytoscape (version: 3.7.1)	(Shannon et al., 2003)	<a href="https://cytoscape.org/">https://cytoscape.org/</a>
CellPhoneDB (version: 1.1.0)	(Vento-Tormo et al., 2018)	<a href="https://github.com/Teichlab/cellphonedb">https://github.com/Teichlab/cellphonedb</a>
HISAT2 (version: 2.1.0)	(Kim et al., 2015)	<a href="https://ccb.jhu.edu/software/hisat2/index.shtml">https://ccb.jhu.edu/software/hisat2/index.shtml</a>

(Continued on next page)

**Continued**

REAGENT or RESOURCE	SOURCE	IDENTIFIER
featureCounts (version: 1.6.4)	(Liao et al., 2014)	<a href="http://subread.sourceforge.net/">http://subread.sourceforge.net/</a>
RcisTarget (version: 1.4.0)	(Verfaillie et al., 2015)	<a href="https://bioconductor.org/packages/release/bioc/html/RcisTarget.html">https://bioconductor.org/packages/release/bioc/html/RcisTarget.html</a>
DESeq2 (version: 1.2.4)	(Love et al., 2014)	<a href="https://bioconductor.org/packages/release/bioc/html/DESeq2.html">https://bioconductor.org/packages/release/bioc/html/DESeq2.html</a>

**LEAD CONTACT AND MATERIALS AVAILABILITY**

Future information and requests for reagents should be directed to and will be fulfilled by lead Guang-Hui Liu ([ghliu@ioz.ac.cn](mailto:ghliu@ioz.ac.cn)).

This study did not generate new unique reagents.

**EXPERIMENTAL MODEL AND SUBJECT DETAILS****Experimental animals**

All experimental procedures were approved by the Chinese Academy of Sciences Institutional Animal Care and Use Committee. The information on age and sex of three groups of rats are as follows: Y-AL (n = 30, 15 male and 15 female rats), O-AL (n = 30, 14 male and 16 female rats), and O-CR (n = 26, 12 male and 14 female rats) groups. Primary rat ASCs were isolated from WAT of 3-month-old female rats. The rats were raised in certificated SPF grade facility with individually ventilated cages. The room was maintained at a controlled temperature (20–25°C), humidity (30%–70%) and light exposure cycle (12 h light-dark cycle).

**Human samples**

Human WAT was collected from healthy peritoneal WAT regions, which was approved by the Peking Union Medical College Hospital Institutional Review Board. Primary human ASCs were isolated from WAT of a 24-year-old woman.

**METHOD DETAILS****Rat strains and feeding plan**

Wild-type *Sprague-Dawley* (SD) rats (strain: CD®(SD) IGS) were ordered from Beijing Vital River Laboratory Animal Technology Co., Ltd., which is joint ventures of Charles River Laboratories in China. The rats were fostered in a specific-pathogen-free (SPF)-grade facility of Beijing Vital River Laboratory Animal Technology before experiments of calorie restriction. At the age of 18 months, the rats were randomly divided into the O-AL (n = 30, 14 male and 16 female rats) and O-CR (n = 26, 12 male and 14 female rats) groups, and transferred to the Institute of Genetics and Developmental Biology, Chinese Academy of Sciences, in a SPF grade facility with individually ventilated cages. The room was maintained at a controlled temperature (20–25°C), humidity (30%–70%) and light exposure cycle (12 h light-dark cycle). According to the baseline food intake, the food intake of the rats was reduced by 10% per week to a final 70% of the AL food intake. Young (5-month-old) and age-matched rats fed AL (O-AL group) were used as controls (Ménard et al., 2014). All experiments were conducted in compliance with animal protocols approved by the Chinese Academy of Sciences Institutional Animal Care and Use Committee.

**Tissue dissociation and cell isolation**

Tissues were isolated from randomly selected Y-AL (5-month-old, n = 6, 3 male and 3 female rats), O-AL (27-month-old, n = 6, 2 male and 4 female rats), and O-CR (27-month-old, n = 6, 3 male and 3 female rats) animals after perfusion with normal saline. The rats were first anesthetized and then the tissues were separated after systemic perfusion with saline through the heart. The same tissues were pooled and quickly minced into ~1-mm<sup>3</sup> pieces on ice in cold PBS (GIBCO), transferred to 15 mL centrifuge tubes and rinsed twice with cold PBS.

WAT, BAT, and kidney tissues were incubated with dissociation buffer containing collagenase I (2 mg/mL) (GIBCO), collagenase IV (2 mg/mL) (GIBCO) and dispase (2 mg/mL) (GIBCO) at 37°C for 1 h (Han et al., 2018). Skin tissues were incubated with dissociation buffer containing collagenase I (1 mg/mL), collagenase IV (1 mg/mL), dispase (1 mg/mL) and trypsin-EDTA (0.125%) (GIBCO) at 37°C for 1 h. Liver tissues were incubated with dissociation buffer containing collagenase IV (1 mg/mL) at 37°C for 40 min. Aortic tissues were first digested with collagenase I (20 mg/mL) for 10 min, followed by incubation with dissociation buffer containing a mixture of collagenase I (2 mg/mL), dispase (2 mg/mL), elastase (2 mg/mL) and DNase I (2.5 U/mL) at 37°C for 30 min (Niederberger et al., 2018).

Digestion of the above six tissue types was terminated by the addition of cold high-glucose DMEM (GIBCO) containing 10% fetal bovine serum (FBS, GIBCO). Dissociated cells were centrifuged at 1,000 rpm and 4°C for 5 min, resuspended in 15 mL of 1 × red blood cell (RBC) lysis buffer (BD Biosciences) at 37°C for 5 min, centrifuged at 1,000 rpm and 4°C for 5 min, washed twice with

cold 1 × PBS and resuspended in 3 mL of cold PBS. The cell suspension was passed through a 40- $\mu$ m strainer (BD Falcon), washed twice with PBS, centrifuged at 1,000 rpm and 4°C for 5 min, and resuspended in cold PBS containing 10% FBS. Dissociated cells were sorted by FACS (BD Influx) to exclude cell debris and counted with a dual fluorescence cell counter (Luna-FL™, Logos Biosystems). The cells were diluted with 0.04% bovine serum albumin (BSA) in PBS to generate a single-cell suspension for 10x Genomics sequencing.

A 5 mL syringe was used to carefully flush out and collect BM from the cavities of the limb bones, femurs and tibias in PBS containing 2% FBS and 2 mM EDTA on ice. The BM suspension was then filtered through a 40- $\mu$ m strainer (BD Falcon) and centrifuged at 1,200 rpm and 4°C for 5 min. The cell pellet was resuspended in 15 mL of 1 × RBC lysis buffer for 5 min and washed twice with cold 1 × PBS before being resuspended in cold 1 × PBS containing 10% FBS. Dissociated cells were sorted by FACS (BD Influx) to exclude cell debris and counted with a dual fluorescence cell counter (Luna-FL™, Logos Biosystems). The cells were diluted with 0.04% BSA in PBS to generate a single-cell suspension for 10x Genomics sequencing.

### Hematoxylin and eosin (H&E) staining

H&E staining was performed as previously described (Kharitonov et al., 2005). Paraffin-embedded tissues were sectioned at a 5- $\mu$ m thickness using a Leica CM3050S cryomicrotome. The sections were mounted onto glass microscope slides, air-dried at 56°C for 24 h and stored at room temperature until use. For H&E staining, the slides were first deparaffinized in xylene and then rehydrated in a graded series of alcohols (100%, 100%, 95%, 80%, 75%) and briefly washed in distilled water. The rehydrated sections were first incubated in hematoxylin until the desired degree of staining was achieved (Servicebio, China) and then washed in running tap water to remove excess solution, differentiated in 1% acid alcohol for 30 s and washed again in running tap water for 1 min. The sections were then counterstained with eosin and dehydrated in a graded series of alcohols and 100% xylene before mounted with Cytoseal-60 (Stephens Scientific).

### Masson's trichrome staining

Paraffin sections were deparaffinized and rehydrated in a graded series of alcohols (100%, 95%, 70%). After being washed in distilled water, the sections were stained with potassium bichromate solution overnight and rinsed with running tap water for 5–10 min. The sections were then stained with Weigert's iron hematoxylin working solution for 10 min, followed by another rinse in running warm tap water for 10 min. Next, the sections were stained with Ponceau-acid fuchsin solution for 5–10 min, washed in distilled water, and differentiated in phosphomolybdic-phosphotungstic acid solution for 10–15 min or until the tissues were no longer red. The sections were then directly transferred (without rinsing) to aniline blue solution and incubated for 5–10 min, followed by a brief rinse in distilled water and differentiation in 1% acetic acid solution for 2–5 min. After a final wash in distilled water, the sections were dehydrated very quickly in 95% ethyl alcohol and absolute ethyl alcohol and cleared in xylene before being mounted with resinous mounting medium.

### SA- $\beta$ -Gal staining

SA- $\beta$ -Gal staining was performed as described previously (Debacq-Chainiaux et al., 2009; Geng et al., 2019; Wang et al., 2020a). Briefly, OCT-embedded, snap frozen, unfixed tissues were cryosectioned at a 10- $\mu$ m thickness using a Leica CM3050S cryomicrotome, collected on Superfrost Plus microslides (VWR) and stored at –80°C until use. For SA- $\beta$ -Gal staining, the sections were thawed and washed in 1 × PBS, fixed with 2% formaldehyde and 0.2% glutaraldehyde at room temperature for 5 min, and stained with freshly prepared staining solution (X-gal, Amresco; all other reagents used for SA- $\beta$ -Gal staining were obtained from Sigma-Aldrich) at 37°C overnight. Images were acquired with an Olympus CKX41 microscope, and the percentages of positive regions were quantified using ImageJ.

### Immunofluorescence microscopy

OCT-embedded, snap frozen, unfixed tissues were cryosectioned at a 10- $\mu$ m thickness using a Leica CM3050S cryomicrotome. Alternatively, cells were seeded on microscope coverslips two days before staining. The slides were washed with PBS, fixed with 4% paraformaldehyde (PFA) in PBS for 30 min and permeabilized with 0.4% Triton X-100 in PBS for 1 h at room temperature. Slides were blocked with blocking buffer (10% donkey serum in PBS) for 1 h at room temperature, followed by incubation at 4°C overnight with primary antibodies diluted in blocking buffer and then at room temperature for 1 h with fluorescence-labeled secondary antibodies diluted in blocking buffer. Three 5-min washes in PBS were performed after each antibody incubation step. Nuclei were counterstained with Hoechst 33342 (Thermo Fisher Scientific). Images were acquired with a Leica SP5 laser scanning confocal microscope, and the percentages of positive regions were quantified using ImageJ.

The following primary antibodies were used for immunofluorescence staining: anti-granulocyte (neutrophil) (ab33760, 1:100) (Reckless et al., 2001), anti-CD68 (ab125212, 1:300) and anti-syndecan-1 (CD138) (ab34164, 1:100) antibodies from Abcam and anti-SMA (ZM-0003, 1:50) and anti-Ki67 (ZM0166, 1:800) antibodies from Zsbio.

### Western blotting

Tissue samples were snap-frozen in cryotubes submerged in liquid nitrogen. For western blot analysis, tissues were ground and lysed with RIPA buffer (0.1% SDS, 50 mM Tris-HCl (pH 7.5), 1% NP-40, 0.5% sodium deoxycholate, and 150 mM NaCl) supplemented with NaVO<sub>4</sub>, NaF and a protease inhibitor mixture (Roche). ASC pellets were also lysed with RIPA buffer. After centrifugation

at 13,000 rpm for 15 min at 4°C, the supernatant was collected and stored at –80°C until use. A BCA kit (Thermo Fisher Scientific) was used for protein concentration measurements. Twenty-five micrograms of protein per sample was separated by SDS-PAGE and transferred to a PVDF membrane (Millipore). Membranes were incubated first with primary antibodies at 4°C overnight and then with HRP-conjugated secondary antibodies at room temperature for 1 h. Quantification was performed with Image Lab software for the ChemiDoc XRS system (Bio-Rad, Hercules, CA).

The following primary antibodies were used for western blotting: anti-LINE1 ORF1p antibody (MABC1152, 1:1,000) from Millipore and anti-GAPDH (ab8245, 1:3,000) and anti-YBX1 (ab12148, 1:1,000) antibodies from Abcam.

### TUNEL staining

TUNEL staining was performed using a TUNEL cell apoptosis detection kit (Roche Molecular Biochemicals) according to the manufacturer's instructions (Wang et al., 2020b). Images were acquired using a Leica SP5 laser scanning confocal microscope, and the percentages of positive cells were quantified using ImageJ.

### Oil Red O staining

Oil Red O staining was performed as described previously (Rojek et al., 2013). In brief, OCT-embedded, snap frozen tissues were cryosectioned at a 10- $\mu$ m thickness using a Leica CM3050S cryomicrotome. Frozen sections were fixed in 10% formalin for 15 min, rinsed in distilled water and air-dried. Frozen sections were then stained with freshly prepared Oil Red O staining solution (Sigma-Aldrich) for 8–10 min at 60°C, differentiated in 85% propylene glycol for 2 min and then rinsed in running tap water. Finally, the sections were counterstained with hematoxylin. Images were acquired in a Leica aperio CS2 system, and the percentages of positive regions were quantified using ImageJ.

### Enzyme-linked immunosorbent assay (ELISA)

The concentrations of S100A8 and TNF $\alpha$  in rat serum were measured with commercial ELISA kits (S100A8: CUSABIO, CSB-EL020641RA; TNF $\alpha$ : Invitrogen, 88-7340) according to the manufacturers' instructions.

### Flow cytometric analysis

Cells isolated from BM were frozen in a solution of 10% DMSO and 90% FBS (GIBCO). After cell recovery, CD8<sup>+</sup> T cells were positively stained with anti-CD3-FITC/anti-CD8-Alexa Fluor 647 monoclonal antibodies for 30 min at 4°C and were then washed twice with PBS. Dead cells were excluded using 7-aminoactinomycin D (7-AAD) for 5 min at room temperature. The analysis was performed on a BD LSRFortessa flow cytometer (BD, USA), and data were further analyzed using FlowJo software.

### Primary ASC culture

Primary human ASCs were isolated from WAT of a 24-year-old woman. This study was approved by the Peking Union Medical College Hospital Institutional Review Board. Primary rat ASCs were isolated from WAT of 3-month-old female rats. ASC isolation was performed according to a previous protocol for rat WAT isolation (see the "Tissue dissociation and cell isolation" section of STAR Methods). The cell suspension in ASC culture medium containing  $\alpha$ -MEM with 1  $\times$  GlutaMAX supplement (GIBCO), 10% FBS (GIBCO), 1% penicillin/streptomycin (GIBCO) and 1 ng/mL bFGF (Joint Protein Central) was added to 0.1% gelatin-coated plates.

### Analysis of cell cycle distribution

After fixation with 70% prechilled ethanol, 1  $\times$  10<sup>6</sup> cells were incubated in staining buffer containing 0.1% Triton X-100, 0.2 mg/mL RNase A and 0.02 mg/mL propidium iodide (PI) at 37°C for 30 min before FACS using a flow cytometer (BD LSRFortessa) and analysis by FlowJo (Cheng et al., 2019).

### Clonal expansion assay

ASCs were seeded into a gelatin-coated 12-well plate at a density of 2,000 cells per well and cultured for nine days. Cells were then fixed with 4% PFA in PBS for 30 min and stained with 0.2% crystal violet (Biohao, China) for 1 h at room temperature. The relative cell density was determined with ImageJ software.

### RNA interference and cell transfection

The *Ybx1* short hairpin RNA (shRNA)-encoding oligonucleotide (CCACGCAATTACCAGCAAA) was cloned into the pLVTHM vector precleaved by ClaI and MluI (NEB) and cotransfected with the packaging plasmids psPAX2 (#12260, Addgene) and pMD2.G (#12259, Addgene) into HEK293T cells. Lentiviral particles were collected from the supernatant of HEK293T cells by ultracentrifugation at 64,300  $\times$  g and 4°C for 135 min and were used to transduce ASCs.

### Nuclear isolation and snRNA-seq on the 10x genomics platform

Fresh frozen brain and skeletal muscle tissues were homogenized in 1 mL of homogenization buffer (250 mM sucrose, 25 mM KCl, 25 mM MgCl<sub>2</sub>, 10 mM Tris buffer, 1  $\mu$ M DTT, 1  $\times$  protease inhibitor, 0.4 U/ $\mu$ L RNaseIn (Thermo Fisher Scientific), 0.4 U/ $\mu$ L Superasin (Thermo Fisher Scientific), 0.1% Triton X-100 (v/v), 1  $\mu$ M PI (Thermo Fisher Scientific), and 10 ng/mL Hoechst 33342 (Thermo Fisher

Scientific) in RNase-free water) using a freezing multisample tissue grinding system (60 Hz, 60 s, 3 times) (TissueLyser-24, Jingxin Industrial Development, China) (Krishnaswami et al., 2016). Samples were passed through a 40- $\mu$ m filter (BD Falcon), centrifuged at 1,000  $\times$  g for 8 min, and resuspended in PBS supplemented with 0.3% BSA (Gemini), 0.4 U/ $\mu$ L RNaseIn and 0.4 U/ $\mu$ L Superasin. Nuclei positive for both Hoechst 33342 and PI were sorted by FACS (BD Influx). Nuclei were counted using a dual fluorescence cell counter (Luna-FL<sup>TM</sup>, Logos Biosystems). The nuclei from the same tissues ( $n = 6$ ) were pooled and diluted to 450–500 nuclei/ $\mu$ l before single-nucleus capture was performed using the 10x Genomics Single-Cell 3' system. Approximately 5,000 nuclei per sample were captured following the standardized 10x capture and library preparation protocol (10x Genomics). To minimize potential batch effects, samples from different groups were loaded on the same 10x chip. Pooled single-nucleus libraries from the individual samples were sequenced in a NovaSeq 6000 Sequencing System (Illumina, 20012866).

### Droplet-based scRNA-seq using the 10x genomics chromium platform

Single cells were encapsulated into droplet emulsions using a Chromium Single-Cell instrument (10x Genomics), and scRNA-seq libraries were constructed following the 10x Genomics protocol using a Chromium Single-Cell 3' Gel Bead and Library V2 Kit. The isolated single cells were then loaded in each channel, with a target output of 5,000 cells per sample. Reverse transcription and library preparation were performed in a Bio-Rad C1000 Touch thermal cycler with a 96-deep-well reaction module. A total of 12 cycles were used for cDNA amplification and the sample index PCR step. Amplified cDNA and final libraries were assessed on a fragment analyzer using a High Sensitivity NGS Analysis Kit (Advanced Analytical). The average fragment length in the 10x cDNA libraries was quantified in a fragment analyzer (AATI) and by qPCR with a Kapa Library Quantification Kit for Illumina. Each individual library was diluted to 2 nM, and pools from equal volumes were sequenced for each run in the NovaSeq 6000 Sequencing System (Illumina 20012866).

## QUANTIFICATION AND STATISTICAL ANALYSIS

### Data processing

Sequencing outputs by the NovaSeq system were demultiplexed using bcl2fastq (version 2.20.0.422) to convert BCL files to FASTQ format. The reads were then aligned to the Rnor\_6.0 genome (for single-nucleus data, we used Cell Ranger software (version 2.2.0) to create the pre-mRNA reference according to the protocol (<https://support.10xgenomics.com/single-cell-gene-expression/software/pipelines/latest/advanced/references>)), and gene counts were calculated by using Cell Ranger with the default parameters to obtain the filtered count matrix for further analysis.

### Clustering and identification of cell types

Calculation of the single-cell and single-nucleus expression matrix by Cell Ranger was performed using the Seurat package (version 2.3.4) for filtering, data normalization, dimensionality reduction, clustering, and gene differential expression analysis (Butler et al., 2018). Before proceeding further, we processed the data with the vignette of DropletUtils (version 1.6.1) package to evaluate the frequency of index swapping (Griffiths et al., 2018). The filtered scRNA-seq and snRNA-seq data were analyzed with the following steps:

1. Cells with fewer than 500 genes detected (or single nuclei with fewer than 300 genes detected) or a mitochondrial gene ratio of greater than 10% (the threshold for kidney cells was a mitochondrial gene ratio of 50%) were excluded.
2. Doublets were detected using the DoubletFinder package (version 2.0.2). The mean-variance-normalized bimodality coefficient (BCMVN) of each sample was calculated to determine the neighborhood size (pK), and the number of artificial doublets (pN) was set to 0.25. Doublets were then detected using the “doubletFinder\_v3” function. The number of doublets for each sample is shown in Table S1.
3. For each cell, the counts were log normalized (1 + counts per 10,000) with the “NormalizeData” function.
4. Variable genes were selected using the “FindVariableGenes” function with the default parameters.
5. Variable genes were projected onto a low-dimensional subspace using canonical correlation analysis (CCA) across samples to correct batch effects by using the “RunMultiCCA” and “AlignSubspace” functions.
6. A shared nearest neighbors graph was constructed based on the Euclidean distance in the low-dimensional subspace spanned by the selected significant principal components. Cells were clustered using the “FindClusters” function at an appropriate resolution.
7. Cells were visualized using a 2-dimensional *t*-distributed stochastic neighbor embedding (*t*-SNE) algorithm with the “RunTSNE” function.
8. Differential expression analysis for each cluster was performed using the Wilcoxon rank-sum test as implemented in the “FindAllMarkers” function.
9. Cell types were assigned to each cluster using the abundance of known marker genes. The details of the expression of the markers for each cell type across the tissues are listed in Table S1.

Through the above pipeline, we processed the scRNA-seq data of 166,111 high-quality from the seven tissues to create a single-cell rat atlas (Data S1A). We identified 109 cell clusters that could be divided into 42 major cell types.

To further understand the changes in the cell types in each tissue, we analyzed the scRNA-seq data for all seven tissues (BAT, WAT, aorta, kidney, liver, skin, and BM) and two snRNA-seq datasets on two additional tissues (brain and skeletal muscle) separately following Steps 1–9 to create the single-cell atlas for each tissue (Data S1B). To obtain more detailed classification of immune cells, we selected *Ptpnc*<sup>+</sup> cells and reclustered them to establish the immune cell atlas for each tissue (except BM) subjected to scRNA-seq. Ultimately, we identified 13 major cell types in BAT based on 28,184 cells, 16 major cell types in WAT based on 30,392 cells, 14 major cell types in liver tissue based on 18,861 cells, 22 major cell types in kidney tissue based on 16,292 cells, 12 major cell types in aortic tissue based on 22,922 cells, 16 major cell types in skin based on 25,662 cells, 15 major cell types in BM based on 23,857 cells, 10 major cell types in brain tissue based on 25,021 cells, and 11 major cell types in skeletal muscle based on 28,131 cells. All subsequent analyses were performed based on data for these cell types among the nine tissues.

### Cell type composition variation analysis

Before analyzing the cell type composition variation, we excluded cell types with fewer than 50 cells identified, only the aortic neutrophils were excluded. The numbers of cells of each type in the different groups (Y-AL, O-AL, and O-CR) were counted and divided by the total number of cells in the same group to calculate the cell type ratio. Based on these ratios, the percentage of a given cell type was calculated for each group. The Log<sub>2</sub>FC between the O-AL and Y-AL groups was then calculated to identify the cell types altered during aging ( $|\text{Log}_2\text{FC}| > 0.5$ ), and the Log<sub>2</sub>FC between the O-CR and O-AL groups was calculated to identify the cell types altered by CR ( $|\text{Log}_2\text{FC}| > 0.5$ ). Accordingly, “rescue CTs” was defined as the cell types that were altered during aging and rescued upon CR.

### Pseudotime analysis

Pseudotime analysis was performed on a filtered subset (tissues with less than 30 neutrophils were excluded) of neutrophils (pro-neutrophils, neutrophils in BM, and peripheral neutrophils in BAT, WAT, liver, and kidney) from the rat atlas data by using the Monocle2 R package (Qiu et al., 2017). Gene ordering was performed by using a cutoff of expression in at least 10 cells and a combination of intercluster differential expression and dispersion with a q-value cutoff of  $< 0.1$ . The structure of the trajectory was plotted in 2-dimensional space using the DDRTree dimensionality reduction algorithm, and the cells were ordered in pseudotime.

### Differential expression and cell-DEG network analyses

Differential expression analysis for each cell type between different groups (O-AL/Y-AL and O-AL/O-CR) was performed using the Wilcoxon rank-sum test as implemented in the “FindMarkers” function of the Seurat package (version 2.3.4). Before executing the differential expression analysis, we filtered out the cell types that were missing or had fewer than three cells in the comparison groups (O-AL/Y-AL and O-CR/O-AL). Accordingly, we excluded B cells, CD8<sup>+</sup> T cells and plasmocytes in the aorta, B cells, NK cells and neutrophils in the kidney, plasmocytes in BAT, and NKTs in skin. First, DEGs between the O-AL and Y-AL groups were identified to generate an aging-related DEG dataset (aging DEGs) ( $|\text{LogFC}| > 0.5$ , adjusted p value  $< 0.05$ ). Secondly, DEGs between the O-CR and O-AL groups were identified to generate a CR-related DEG dataset (CR DEGs) ( $|\text{LogFC}| > 0.5$ , adjusted p value  $< 0.05$ ). Based on the above results, “rescue DEGs” were defined as the upregulated or downregulated genes among the aging DEGs that were downregulated or upregulated, respectively, upon CR; “side-effect DEGs” were defined as the upregulated or downregulated genes among the aging DEGs that were further upregulated or downregulated, respectively, upon CR; and “CR-specific DEGs” were defined as the upregulated or downregulated genes among the CR DEGs that were not markedly changed during aging. Next, cell-DEG networks for each set of the aforementioned DEGs from the scRNA-seq data were established by integrating the tissue and cell type source of the DEGs and the LogFC values of related genes. The cell-DEG networks were visualized with Cytoscape (version 3.7.1) (Shannon et al., 2003). In addition, DEGs ( $|\text{LogFC}| > 0.5$ , adjusted p value  $< 0.05$ ) between the O-CR and Y-AL groups were identified to compare the rescue effect between the aging and CR DEGs.

### GO analysis

GO biological process and pathway enrichment analyses were performed using Metascape (version 3.5) (Zhou et al., 2019) (<http://metascape.org>), and the results were visualized with the ggplot2 R package ( $p < 0.01$ ) (Wickham, 2016). A total of 10 GO terms related to aging and/or CR out of the top 30 enriched GO terms across multiple tissues/cell types were displayed. Heatmaps and gene expression profile cluster plots were obtained using the pheatmap R package. Graphics were generated with ggplot2, and figures were prepared with Inkscape.

### Transcription factor-target gene network analysis

Core regulatory transcription factors were predicted based on the scRNA-seq data. Transcription factor-binding motifs were identified via the GENIE3 R/Bioconductor packages (version 1.6.0) (Huynh-Thu et al., 2010) and the RcisTarget database (version 1.4.0) (Verfaillie et al., 2015) of the SCENIC (version 1.1.2.2) (Aibar et al., 2017) workflow using default parameters (<http://scenic.aertslab.org/>). GENIE3 was used to infer gene regulatory networks from gene expression matrices of each tissue and set of aging DEGs, CR DEGs or rescue DEGs for each cell type. RcisTarget was used to identify enriched transcription factor-binding motifs and to predict candidate target genes (regulons) based on the mm9 RcisTarget database containing motifs with genome-wide rankings. Only the transcription factor targets with high-confidence annotation were visualized with Cytoscape (version 3.7.1) (Shannon et al., 2003).

### Cell-cell communication analysis

Cell-cell communication was predicted based on the scRNA-seq data by using CellPhoneDB software (version 1.1.0) ([www.cellphonedb.org](http://www.cellphonedb.org)) (Vento-Tormo et al., 2018). Only receptors and ligands expressed in at least 10% of cells of a given type were further analyzed, whereas the interaction was considered nonexistent if either the ligand or the receptor was undetectable. The average expression of each ligand-receptor pair was compared between different cell types, and only those with  $p < 0.05$  were used for subsequent prediction of cell-cell communication in the three groups (Y-AL, O-AL, and O-CR) for each tissue.

### Bulk RNA-seq analysis

RNA-seq data processing was performed as previously described (Geng et al., 2019; Wang et al., 2020a). Briefly, after quality control and adaptor trimming, sequencing reads were mapped to the UCSC human hg19 genome with HISAT2 software (version 2.1.0) (Kim et al., 2015). The featureCounts (version 1.6.4) function was used to determine the expression level of each annotated gene (Liao et al., 2014). DEGs were identified using DESeq2 (version 1.2.4) (Love et al., 2014) as those with a cutoff Benjamini-Hochberg adjusted  $p$  value of 0.05 and an absolute fold change of greater than 1.5 ( $|\text{Log}_2\text{FC}| > 0.58$ ). The Euclidian distance was calculated using R to evaluate the correlation between the replicates of each sample based on DESeq2 regularized logarithm (rlog)-normalized read count. The gene expression levels (FPKM) in each sample were then calculated using custom scripts.

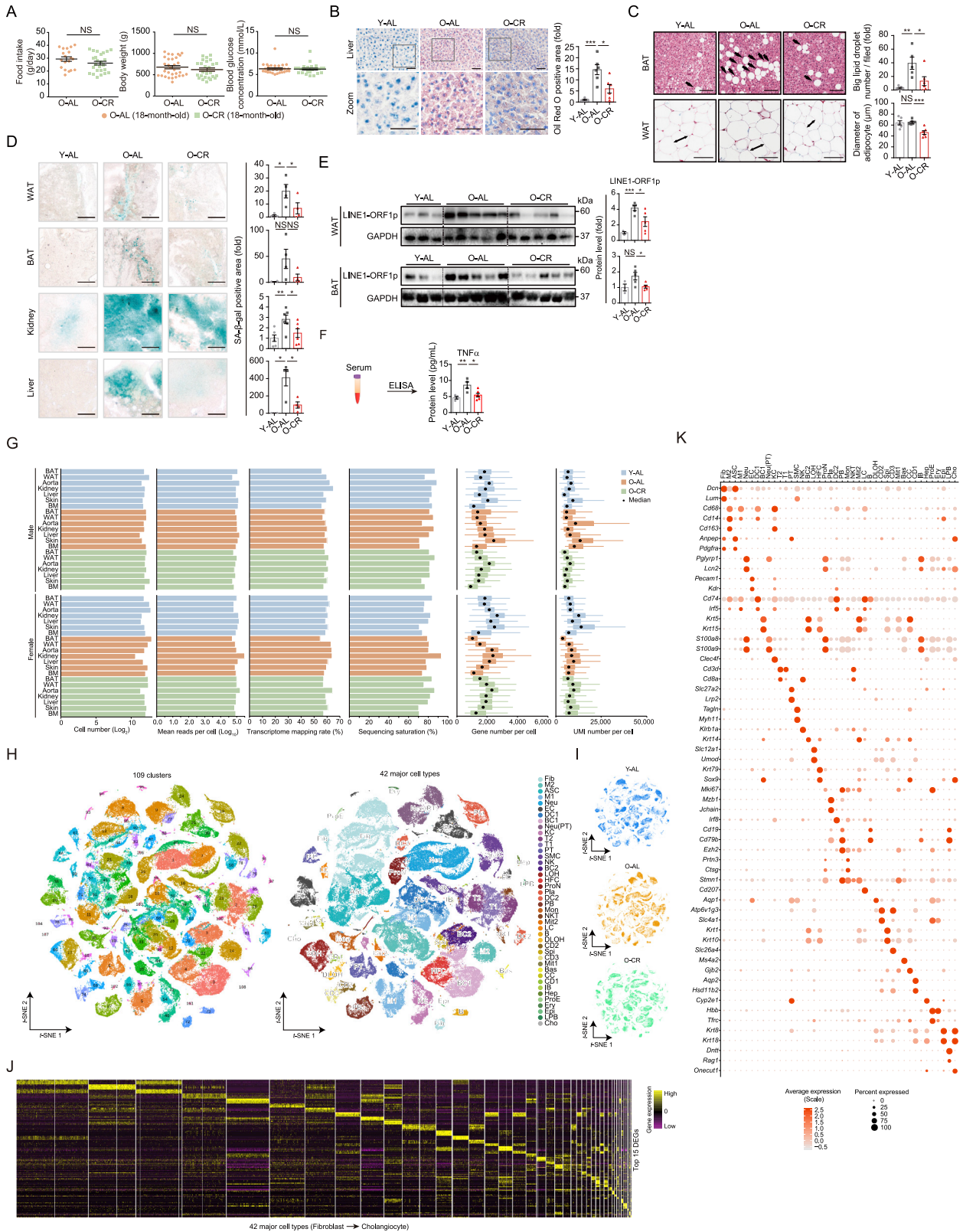
### Statistical analysis

Data are presented as means  $\pm$  SEM. Statistical analyses were performed using a two-tailed Student's  $t$  test in PRISM software (GraphPad 6 Software) to compare the differences between treatment and control groups assuming equal variance.  $p < 0.05$  is considered statistically significant. \*, \*\*, \*\*\* and \*\*\*\* indicate  $p < 0.05$ ,  $p < 0.01$ ,  $p < 0.001$  and  $p < 0.0001$ , respectively. NS indicates not significant.

### DATA AND CODE AVAILABILITY

The accession number for the RNA-seq sequencing and processed data reported in this paper is GEO: GSE137869. Scripts reproducing the analysis are available at <https://github.com/MSZaki/Aging-and-CR-rat-atlas>.

# Supplemental Figures



(legend on next page)

**Figure S1. Morphological and Histological Characterizations of Aging and CR Rats and scRNA-seq Data Quality Control and Cell Type Identification across Seven Tissues, Related to Figure 1**

(A) Food intake (g/day), body weight (g) and blood glucose concentration (mmol/L) of rats before calorie-restricted diet feeding (O-AL: n = 30, 14 male and 16 female rats; O-CR: n = 26, 12 male and 14 female rats). Each dot represents one rat. O-AL (18-month-old), O-AL group before calorie-restricted diet feeding. O-CR (18-month-old), O-CR group before calorie-restricted diet feeding. The data are shown as means  $\pm$  SEM. NS, not significant.

(B) Oil Red O staining analysis of livers from each group, as indicated (n = 5–6 per group). The data are shown as means  $\pm$  SEM. \*\*\*p < 0.001; \*p < 0.05. Scale bars, 100  $\mu$ m.

(C) H&E staining of rat BAT (n = 5–6 per group) (top panel). The unidirectional arrows indicate large lipid droplets with a diameter of at least 40  $\mu$ m. Masson's trichrome staining of WAT (n = 6 per group) (bottom panel). The bidirectional arrow indicates the diameter of the cells. The data are shown as means  $\pm$  SEM. \*\*\*p < 0.001; \*\*p < 0.01; \*p < 0.05; NS, not significant. Scale bars, 100  $\mu$ m.

(D) SA- $\beta$ -Gal staining analysis of WAT, BAT, kidney tissues and liver tissues (n = 4 per group). The data are shown as means  $\pm$  SEM. \*\*p < 0.01; \*p < 0.05; NS, not significant. Scale bars, 100  $\mu$ m.

(E) Immunoblot analysis of LINE1-ORF1p as indicated in WAT or BAT of Y-AL (n = 3), O-AL (n = 5) and O-CR (n = 5) rats. The data are shown as means  $\pm$  SEM. \*\*\*p < 0.001; \*p < 0.05; NS, not significant.

(F) ELISA of TNF $\alpha$  in the serum of Y-AL (n = 4), O-AL (n = 4) and O-CR (n = 6) rats. The data are shown as means  $\pm$  SEM. \*\*p < 0.01; \*p < 0.05.

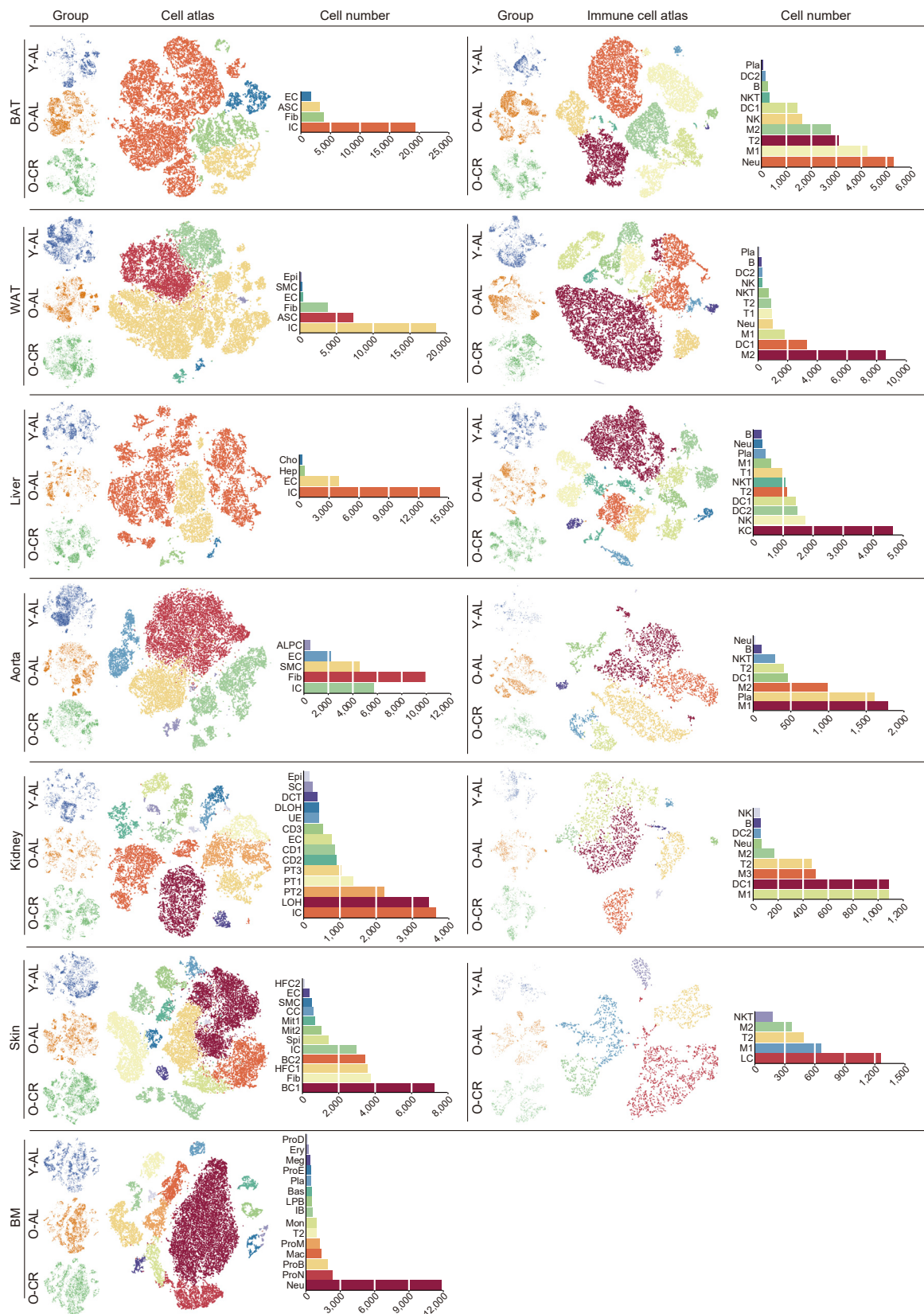
(G) Cell number, mean reads per cell, transcriptome mapping rate, sequencing saturation, gene number and unique molecular identifier (UMI) number per cell for the scRNA-seq data in the three groups across the seven tissues of female and male rats.

(H) t-SNE plots showing different clusters (left panel) and cell types (right panel) across the seven tissues. A total of 109 clusters are divided into 42 major cell types. The full names of the 42 major cell types are as follows: Fib, Fibroblast; M2, Macrophage II; ASC, Adipose-derived stem cell; M1, Macrophage I; Neu, Neutrophil; EC, Endothelial cell; DC1, *Irf8*<sup>-</sup> Dendritic cell; BC1, *Krt15*<sup>+</sup> Basal cell; Neu (PT), Neutrophil (peripheral tissues); KC, Kupffer cell; T2, CD8<sup>+</sup> T cell; T1, CD4<sup>+</sup>CD8<sup>-</sup> T cell; PT, Proximal tubule; SMC, Smooth muscle cell; NK, Natural killer cell; BC2, *Krt14*<sup>+</sup> Basal cell; LOH, Thick ascending limb of the loop of Henle; HFC, Hair follicle cell; ProN, Pro-neutrophil; Pla, Plasmocyte; DC2, *Irf8*<sup>+</sup> Dendritic cell; PB, Pro-B cell; Mon, Monocyte; NKT, Natural killer T cell; Mit2, Mitotic cell 2; LC, Langerhans cell; B, B cell; DLOH, Descending loop of Henle; CD2, Intercalated cell of the collecting duct, type A; Spi, Spinous cell; CD3, Intercalated cell of the collecting duct, type B; Mit1, Mitotic cell 1; Bas, Basophil; CC, Channel cell; CD1, Principal cell of the collecting duct; IB, Immature B cell; Hep, Hepatocyte; ProE, Pro-erythroblast; Ery, Erythroblast; Epi, Epithelial cell; LPB, Late pro-B cell; Cho, Cholangiocyte.

(I) t-SNE plots showing the sampling information. The three groups (Y-AL, O-AL, and O-CR) are marked in different colors.

(J) Heatmap showing the top 15 DEGs (sorted by adjusted p value, with an adjusted p value of < 0.05) (column) in each cell type (row). The color key from purple to yellow indicates gene expression levels from low to high.

(K) Dot plots showing the expression levels of specific marker genes for each cell type. The information on marker genes for each cell type is shown in [Table S1](#).

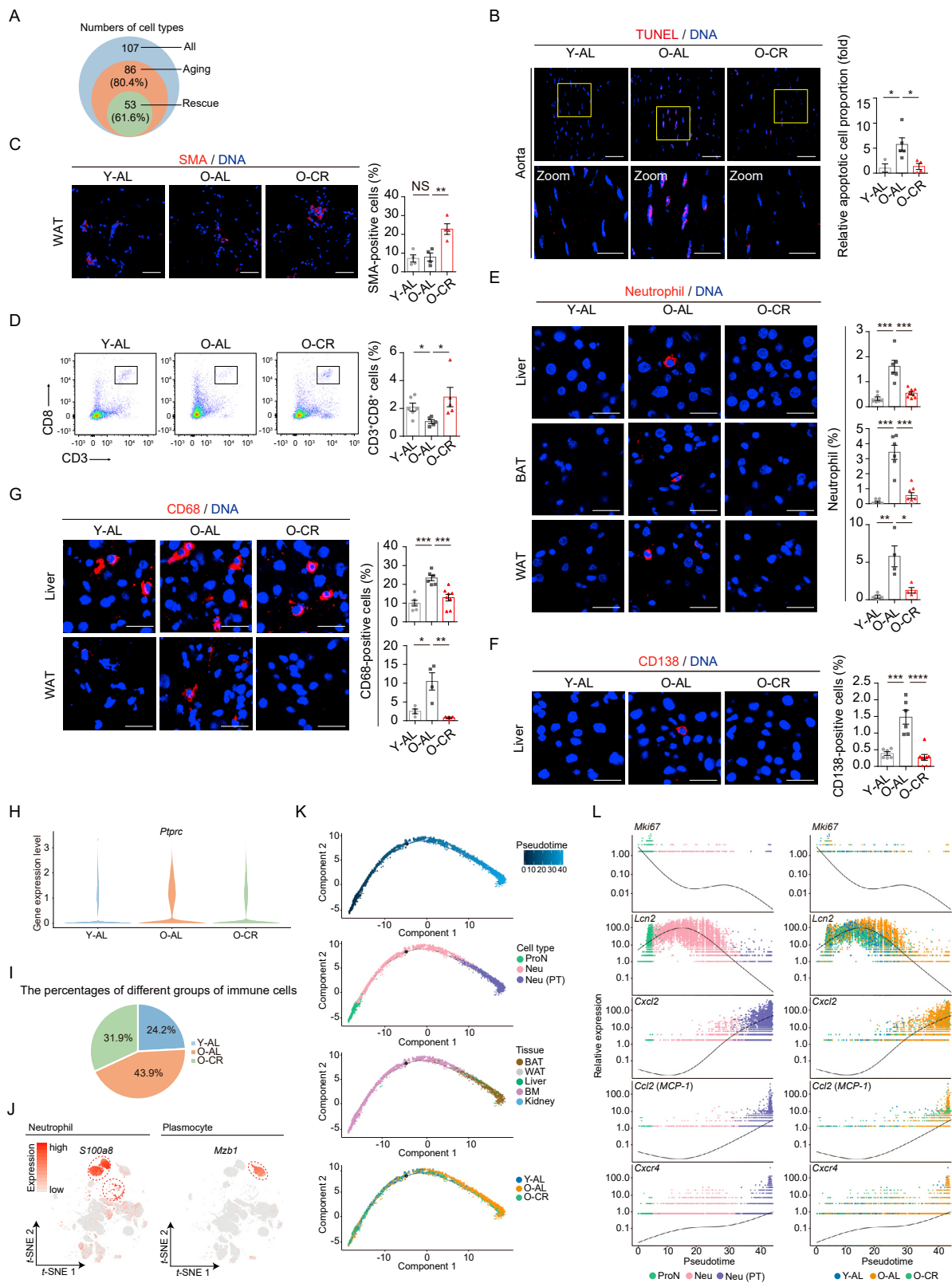


(legend on next page)

---

**Figure S2. Diversity and Complexity of Total Cell Types among Each Tissue, Related to [Figure 2](#)**

t-SNE plots showing the cell atlases of all cell types (left panel) and immune cell types (right panel) in each tissue among the three groups (Y-AL, blue; O-AL, orange; O-CR, green). Cell types were identified by differential gene expression of known markers between clusters. The bar plots indicate the numbers of cells of each annotated type.



(legend on next page)

---

**Figure S3. Changes in the Composition of Key Cell Types during Aging and CR, Related to Figure 2**

(A) Venn diagrams showing the number of cell types whose proportions were changed during aging and rescued by CR. All, the total number of cell types in seven tissues. Aging, the number of cell types whose proportions were altered during aging ( $|\text{Log}_2\text{FC}| > 0.5$ ). Rescue, the number of cell types whose proportions were changed during aging and reversed upon CR ( $|\text{Log}_2\text{FC}| > 0.5$ ).

(B) TUNEL staining of aortas from Y-AL (n = 3), O-AL (n = 5) and O-CR (n = 4) rats. The data are shown as the means  $\pm$  SEM ( $\geq 300$  cells quantified per individual). \* $p < 0.05$ . Scale bars, 50  $\mu\text{m}$  (Zoom, 25  $\mu\text{m}$ ).

(C) Immunostaining of SMA in rat WAT (n = 4 per group). The data are shown as the means  $\pm$  SEM ( $\geq 300$  cells quantified per individual). Data are shown as the means  $\pm$  SEM. \*\* $p < 0.01$ ; NS, not significant. Scale bars, 50  $\mu\text{m}$ .

(D) Flow cytometric analysis of CD3<sup>+</sup>CD8<sup>+</sup> cells from BM. The data are shown as means  $\pm$  SEM. \* $p < 0.05$ .

(E) Immunostaining of neutrophils in the liver (n = 6–8), BAT (n = 6–8) and WAT (n = 4) of each group. The data are shown as means  $\pm$  SEM ( $\geq 300$  cells quantified per individual). \*\*\* $p < 0.001$ ; \*\* $p < 0.01$ ; \* $p < 0.05$ . Scale bars, 25  $\mu\text{m}$ .

(F) Immunostaining of plasmocyte marker CD138 in rat livers (n = 6–8 per group). The data are shown as means  $\pm$  SEM ( $\geq 300$  cells quantified per individual). \*\*\* $p < 0.001$ ; \*\*\*\* $p < 0.0001$ . Scale bars, 25  $\mu\text{m}$ .

(G) Immunostaining of macrophage marker CD68 in rat livers and WAT (n = 6–8 per group). The data are shown as means  $\pm$  SEM ( $\geq 300$  cells quantified per individual). \*\*\* $p < 0.001$ ; \*\* $p < 0.01$ ; \* $p < 0.05$ . Scale bars, 25  $\mu\text{m}$ .

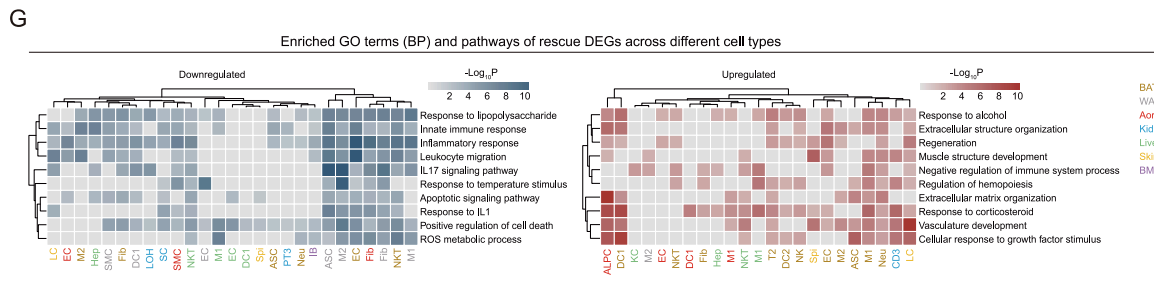
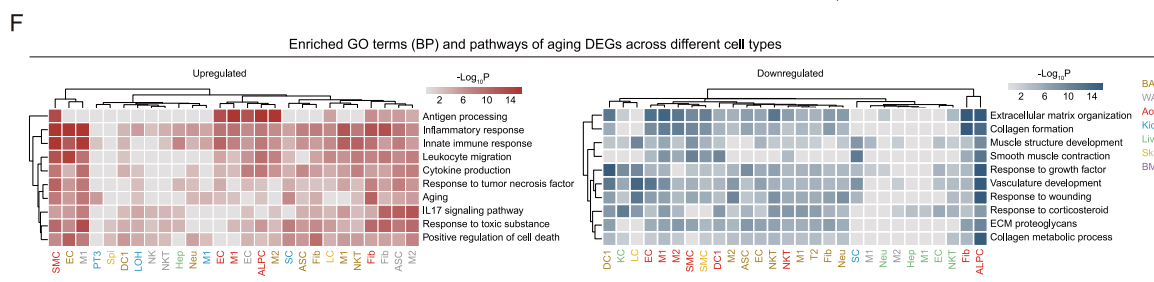
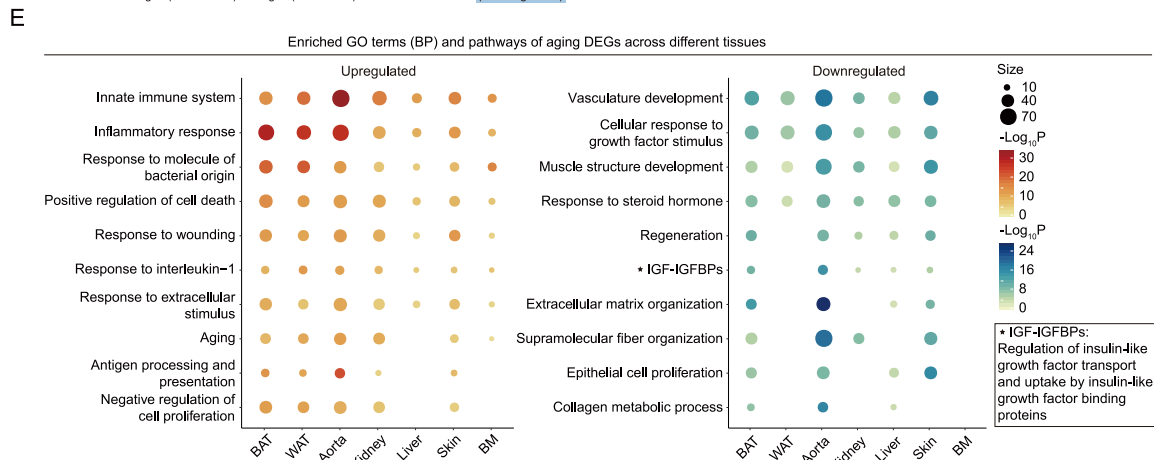
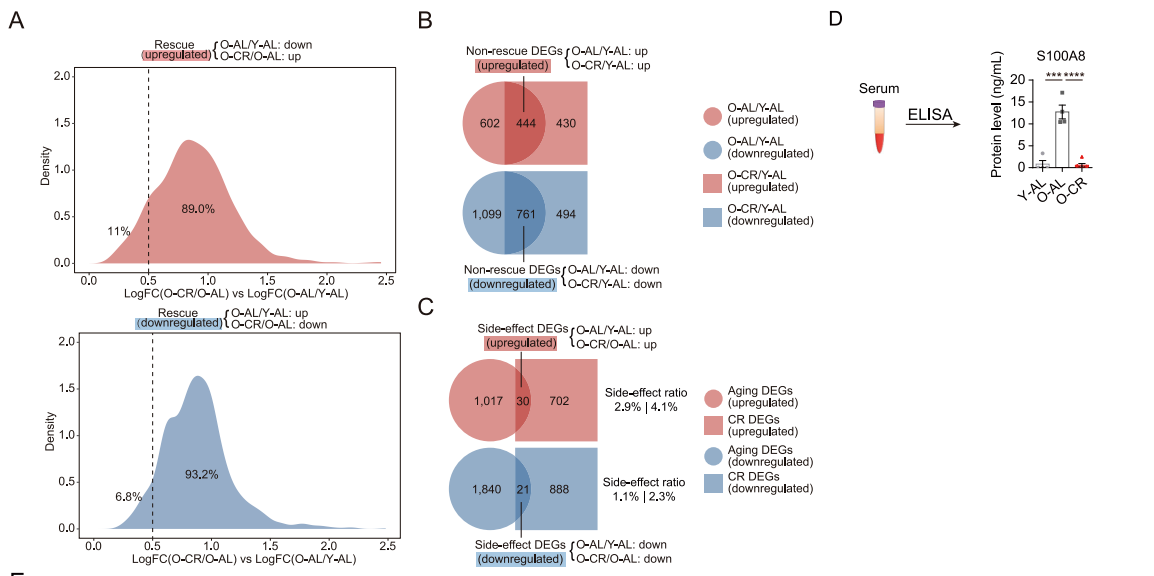
(H) Violin plots showing the expression levels of immune cell marker *Ptprc*<sup>+</sup> in multiple tissues except for BM from the three groups (Y-AL, O-AL, and O-CR).

(I) Pie chart showing the relative percentages of immune cells (*Ptprc*<sup>+</sup> cells) in multiple tissues except for BM whose proportions were changed during aging and rescued by CR.

(J) *t*-SNE plots showing the cell-type-specific markers for neutrophils (left panel) and plasmocytes (right panel) in the same layout used in Figure 2C. The color key from gray to red indicates gene expression levels from low to high.

(K) Pseudotime trajectory analysis corresponding to the differentiation of neutrophils from pro-neutrophils in BM to neutrophils in BM to tissue-infiltrating neutrophils. Cells are colored by pseudotime, cell type, tissue type or group name, as indicated, from the top to the bottom panels.

(L) The relative gene expression patterns of the indicated markers over pseudotime. Cells are colored by cell type or group name. The horizontal axis indicates the pseudotime value, and the vertical axis indicates the relative gene expression value.



(legend on next page)

---

**Figure S4. Analyses of Aging, CR, and Rescue DEGs across Tissues, Related to Figure 4**

(A) Density plots showing the distribution density of the rescue efficiency ratios for the DEGs of all cell types among seven tissues between the O-AL/Y-AL and O-CR/O-AL comparison groups.

(B) Venn diagrams showing the numbers of DEGs between the O-AL/Y-AL and O-CR/Y-AL comparison groups. The overlapping regions represent the numbers of non-rescue DEGs.

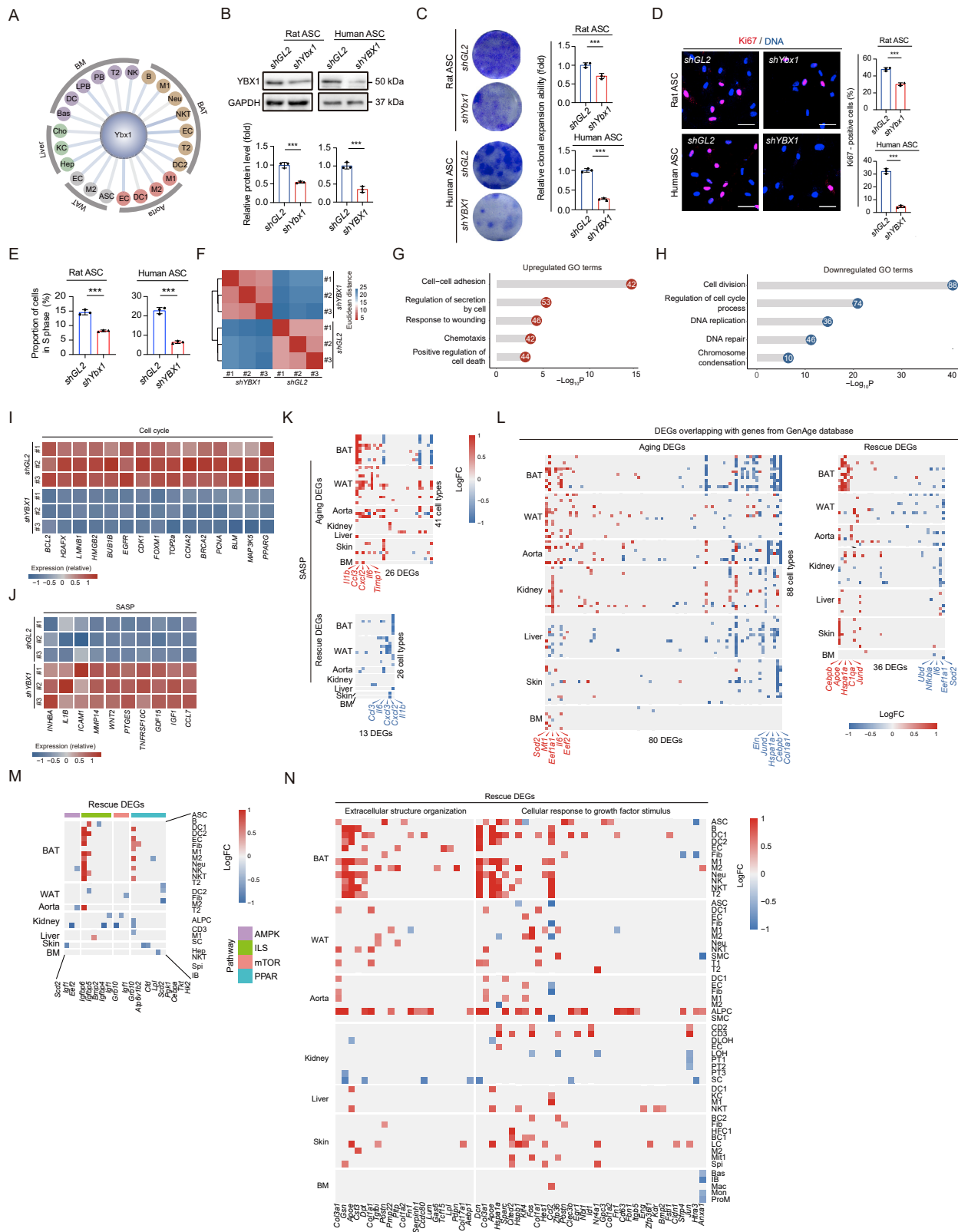
(C) Venn diagrams showing the numbers of aging DEGs whose change in expression was enhanced by CR. The overlapping regions represent the numbers of upregulated aging DEGs whose change in expression was enhanced by CR (upregulated during aging and further upregulated by CR) (top) and downregulated aging DEGs whose change in expression was enhanced by CR (downregulated during aging and further downregulated by CR) (bottom).

(D) ELISA of S100A8 in the serum of Y-AL (n = 4), O-AL (n = 4) and O-CR (n = 6) rats. The data are shown as means  $\pm$  SEM. \*\*\*p < 0.001; \*\*\*\*p < 0.0001.

(E) GO term and pathway enrichment analyses of aging DEGs across different tissues. Red indicates the upregulated pathways, and blue indicates the downregulated pathways (p < 0.01). The sizes of the circles correspond to the number of genes enriched in each term.

(F) GO terms and pathways of the aging DEGs across the top 30 cell types based on their aging DEG numbers. The color key from red to gray indicates p values (p < 0.01) from low to high, and the color key from blue to gray indicates p values (p < 0.01) from low to high. Different types of cells are colored by tissue type and annotated to the right.

(G) GO terms and pathways of the aging DEGs across the top 30 cell types based on their rescue DEG numbers. The color key from red to gray indicates p values (p < 0.01) from low to high, and the color key from blue to gray indicates p values (p < 0.01) from low to high. Different types of cells are colored by tissue type and annotated to the right.



(legend on next page)

**Figure S5. Verification of Ybx1 as a Newly Identified Aging-Related Key Factor and Changes in the Expression of Genes Related to Aging and Nutrient-Sensing Pathways during Aging and CR, Related to Figure 5**

- (A) Network showing the cell types with *Ybx1*-associated downregulation during aging. The gradation of blue in the line indicates the fold downregulation of *Ybx1* by the LogFC value. Cells are colored by tissue type as indicated.
- (B) Verification of the knockdown efficiency of lentiviral sh*Ybx1* vector in both rat and human ASCs by western blotting ( $n = 3$ ). The data are shown as means  $\pm$  SEM. \*\*\* $p < 0.001$ .
- (C) Clonal expansion assay of ASCs transduced with lentiviral vectors expressing *shGL2* or *shYbx1* ( $n = 3$ ). Left, representative images of crystal violet staining. Right, the relative intensity of crystal violet staining as quantified by ImageJ. The data are shown as means  $\pm$  SEM. \*\*\* $p < 0.001$ .
- (D) Ki67 immunostaining analysis of ASCs transduced with lentiviral vectors expressing *shGL2* or *shYbx1*. The data are shown as means  $\pm$  SEM. More than 300 cells were analyzed for each group. \*\*\* $p < 0.001$ . Scale bars, 50  $\mu\text{m}$ .
- (E) Cell cycle analysis of ASCs transduced with lentiviral vectors expressing *shGL2* or *shYbx1* ( $n = 3$ ). The data are shown as means  $\pm$  SEM. \*\*\* $p < 0.001$ .
- (F) Heatmaps showing the pairwise Euclidean distance between each sample (bulk RNA-seq data).
- (G) GO analysis of upregulated DEGs in the *shYbx1* group compared to the *shGL2* group (bulk RNA-seq data). The number in the circle corresponds to the number of genes enriched in each term.
- (H) GO analysis of downregulated DEGs in the *shYbx1* group compared to the *shGL2* group (bulk RNA-seq data). The number in the circle corresponds to the number of genes enriched in each term.
- (I) Heatmaps showing downregulation of cell cycle-related DEGs in the *shYbx1* group compared to the *shGL2* group (bulk RNA-seq data). The color key from blue to red indicates relative gene expression levels from low to high.
- (J) Heatmaps showing the upregulation of SASP-related DEGs in the *shYbx1* group compared to the *shGL2* group (bulk RNA-seq data). The color key from blue to red indicates relative gene expression levels from low to high.
- (K) Heatmaps showing the expression levels of aging DEGs (left) and rescue DEGs (right) among SASP-related genes in different cell types across different tissues. The rows represent cell types, and the columns represent genes. The color key from blue to red indicates low to high LogFC of DEGs, respectively. The top five DEGs are listed in the bottom.
- (L) Heatmaps showing the expression levels of aging (left) or rescue (right) DEGs among genes from the GenAge database in different cell types across the seven tissues. The rows represent cell types, and the columns represent DEGs. The color key from blue to red indicates low to high LogFC of DEGs, respectively. The top five DEGs are listed in the bottom.
- (M) Heatmaps showing the expression levels of rescue DEGs involved in the indicated nutrient-sensing pathways in different cell types across different tissues. The rows represent cell types, and the columns represent genes. The color key from blue to red indicates low to high LogFC of DEGs, respectively. The different colors of the bars denote the indicated pathways. AMPK, AMP-activated protein kinase signaling pathway; ILS, insulin-like signaling pathway; mTOR, mammalian target of rapamycin signaling pathway; PPAR, peroxisome proliferator-activated receptor signaling pathway.
- (N) Heatmaps showing the expression levels of rescue DEGs classified in structure- and growth-related GO terms in different cell types across different tissues. The rows represent cell types, and the columns represent genes. The color key from blue to red indicates low to high LogFC of DEGs, respectively.

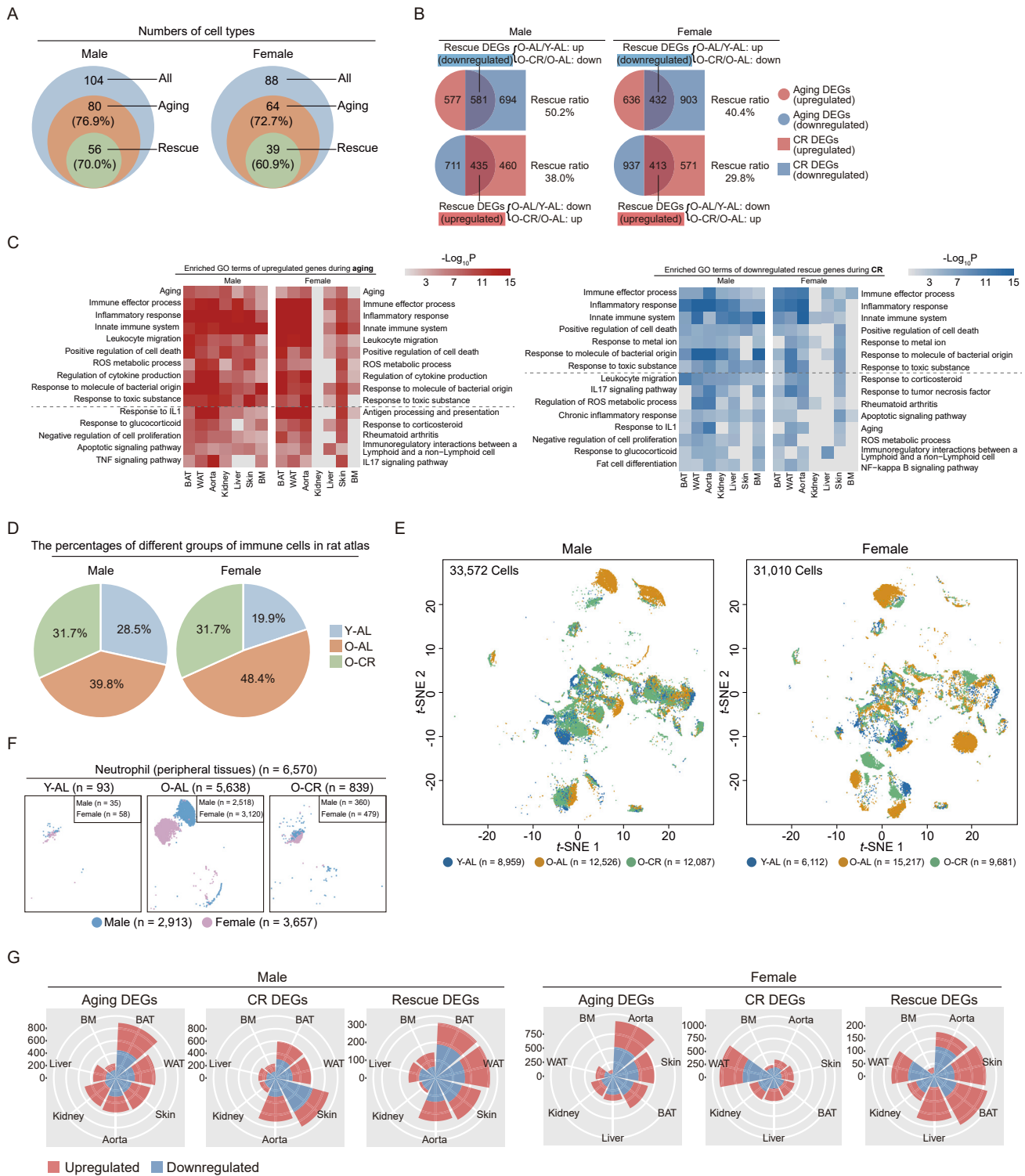


**Figure S6. Changes in the Cell Type Composition and Transcriptional Profiles between the Different Sexes during Aging and CR, Related to “Cell Type Composition Variation Analysis” and “Differential Expression and Cell-DEG Network Analyses” in STAR Methods**

(A) Venn diagrams showing the number of cell types whose proportions were changed during aging and rescued by CR in male and female rats. All, the total number of cell types in the seven tissues. Aging, the number of cell types whose proportions were altered during aging ( $|\text{Log}_2\text{FC}| > 0.5$ ). Rescue, the number of cell types whose proportions were changed during aging and reversed by CR ( $|\text{Log}_2\text{FC}| > 0.5$ ).

(legend continued on next page)

---

(B) Venn diagrams showing the numbers of rescue DEGs in male and female rats. The overlapping regions indicate the numbers of downregulated rescue DEGs (upregulated during aging and downregulated by CR) (top) and upregulated rescue DEGs (downregulated during aging and upregulated by CR) (bottom).

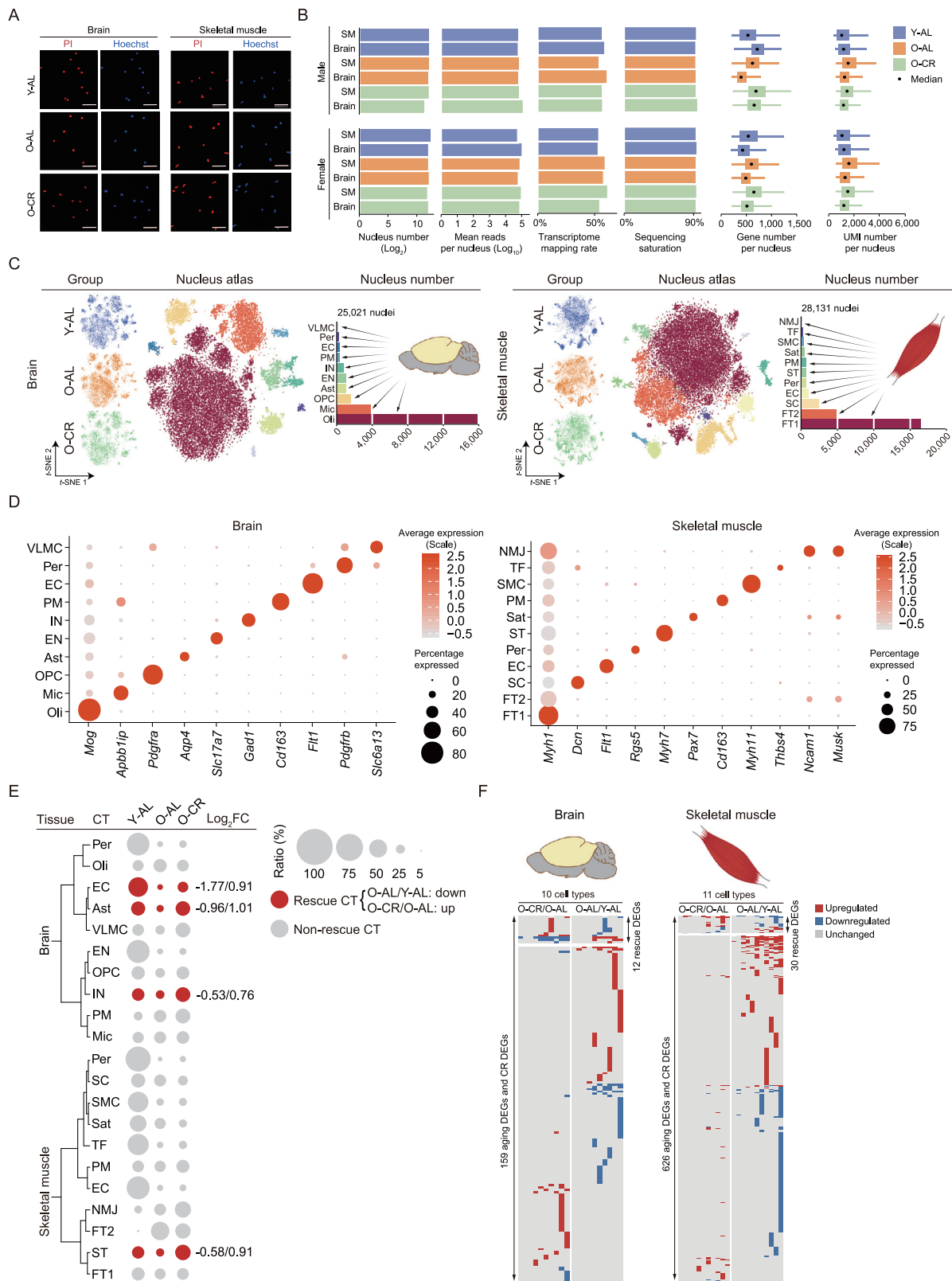
(C) Representative GO terms and pathways enriched in rescue DEGs based on functional enrichment analysis in male and female rats. Red indicates the most significantly upregulated GO terms, and blue indicates the most significantly downregulated GO terms ( $p < 0.01$ ).

(D) Pie chart showing the relative percentages of immune cells ( $Ptprc^+$ ) in male and female rats of the indicated groups.

(E) *t*-SNE plots showing that immune cells ( $Ptprc^+$ ) accumulated in O-AL tissues. *t*-SNE plots of immune cells in the Y-AL, O-AL and O-CR groups. The number of  $Ptprc^+$  immune cells in male and female rats of each group is labeled.

(F) *t*-SNE plots showing the numbers of neutrophils in male and female rats of the indicated groups (Y-AL, O-AL, and O-CR). Cells are colored by sex. The numbers of neutrophils in rats of each sex are denoted at the corner of the plot.

(G) Rose diagrams showing the numbers of aging DEGs, CR DEGs and rescue DEGs in the seven tissues of male and female rats. Red indicates upregulated, and blue indicates downregulated.



(legend on next page)

**Figure S7. Changes in Cell Type Composition and Transcriptional Profiles in the snRNA-Seq Data of Brain and Skeletal Muscle during Aging and CR, Related to “Nuclear Isolation and snRNA-Seq on the 10x Genomics Platform” in STAR Methods**

(A) Cell nuclei extracted from the brain and skeletal muscle of rats in the three groups. Scale bars, 50  $\mu\text{m}$ . DNA was counterstained by Hoechst 33342 and PI.

(B) Nucleus number, mean reads per nucleus, transcriptome mapping rate, sequencing saturation, gene number, and UMI number for the snRNA-seq data across the brain and skeletal muscle of female and male rats of the three groups.

(C) *t*-SNE and bar plots showing the cell atlas and the number of different cell types in the brain tissue (left) and skeletal muscle (right) of the three groups (Y-AL, blue; O-AL, orange; and O-CR, green). The full names of the 18 major cell types are as follows: VLMC, Vascular leptomeningeal cell; Per, Pericyte; EC, Endothelial cell; PM, Perivascular macrophage; IN, Inhibitory neuron; EN, Excitatory neuron; Ast, Astrocyte; OPC, Oligodendrocyte progenitor cell; Mic, Microglia; Oli, Oligodendrocyte; NMJ, Neuromuscular junction-postsynaptic muscle fiber; TF, Tendon fibroblast; SMC, Smooth muscle cell; Sat, Satellite cell; ST, Slow-twitch muscle fiber, type I; SC, Stromal cell; FT2, Fast-twitch muscle fiber, type IIA; FT1, Fast-twitch muscle fiber, type IIX.

(D) The marker genes of different cell types in the brain (left) and skeletal muscle (right).

(E) Relative changes in cell ratios in the brain (left) and skeletal muscle (right) across the three groups (Y-AL, O-AL, and O-CR). Each circle represents the relative cell ratio. The red circle denotes cell ratios lower in the O-AL group than in the Y-AL group and higher in the O-CR group than in the O-AL group ( $|\text{Log}_2\text{FC}| > 0.5$ ); the gray circle denotes cell ratios not markedly rescued by CR ( $|\text{Log}_2\text{FC}| < 0.5$ ). The numbers on the right indicate the  $\text{Log}_2\text{FC}$  values of the cell ratios (O-AL/Y-AL and O-CR/O-AL). FC, fold change.

(F) Heatmaps showing the distribution of DEGs in each cell type in the brain and skeletal muscle. Each row indicates one cell type, and each column indicates one gene. Red, upregulated ( $\text{LogFC} > 0.5$ , adjusted  $p$  value  $< 0.05$ ); blue, downregulated ( $\text{LogFC} > 0.5$ , adjusted  $p$  value  $< 0.05$ ); gray, unchanged ( $|\text{LogFC}| < 0.5$ ). The numbers of rescue DEGs are shown at the top of each heatmap. Aging DEGs are the genes that were changed in the O-AL group compared to the Y-AL group in each cell type. CR DEGs are the genes that were changed in the O-CR group compared to the O-AL group in each cell type. Rescue DEGs are the genes that exhibited the opposite changes in CR DEGs compared to aging DEGs in each cell type.